

An EWPD SMEFT likelihood for the LHC — and how to improve it with measurements of W and Z boson properties

Hannes Mildner

*Johannes Gutenberg-Universität Mainz,
Staudingerweg 7, 55128 Mainz, Germany*

E-mail: hannes.mildner@cern.ch

ABSTRACT: This paper presents a computer code for analyzing electroweak precision data (EWPD) in the framework of the Standard Model Effective Field Theory (SMEFT), highlights the importance of recent ATLAS and CMS precision measurements, and introduces a novel analysis of the forward–backward asymmetry at the LHC. The computer code provides the likelihood of SMEFT Wilson coefficients based on precision measurements of W and Z pole observables, interpolation formulas for Standard Model predictions, and modular SMEFT parametrizations. SMEFT predictions including next-to-leading-order (NLO) effects in perturbative and SMEFT expansion are available and five alternative electroweak input parameter schemes are supported. The likelihood addresses shortcomings of previous formulations in the treatment of parametric uncertainties and can be straightforwardly included in SMEFT fits of LHC data. The input parameter scheme dependence and role of NLO corrections is studied for the EWPD fit in the SMEFT. Furthermore, the impact of recent ATLAS and CMS measurements — of the W boson mass and width, of the lepton flavour universality (LFU) of W branching fractions, and the effective leptonic weak mixing angle, $\sin^2 \theta_{\text{eff}}^\ell$ — is analyzed. A test of LFU that surpasses the precision other tests is proposed based on the $\sin^2 \theta_{\text{eff}}^\ell$ measurement. Finally, an ATLAS Drell–Yan triple-differential cross-section measurement is reinterpreted in the SMEFT and combined with the EWPD likelihood. This analysis demonstrates the feasibility of the LFU precision test, improves constraints on muon couplings with respect to the world average, and determines a combination of the quark-coupling asymmetry parameters A_u and A_d with a precision close to the heavy flavour parameters A_c and A_b .

Contents

1	An EWPD SMEFT likelihood for the LHC	3
1.1	Input observables	4
1.2	SM predictions	6
1.3	Treatment of uncertainties	7
1.4	The EWPD fit in the SM	9
1.5	SMEFT parametrization	11
1.6	The EWPD fit in the SMEFT (at NLO)	14
2	Impact of recent LHC measurements on the EWPD likelihood	18
2.1	ATLAS measurement of W boson mass and width	18
2.2	ATLAS measurement of lepton flavour universality in W decays	22
2.3	CMS measurement of the effective leptonic weak mixing angle	23
2.4	Comparison of lepton flavour universality tests	25
3	Interpretation of the ATLAS Drell–Yan triple-differential cross-section measurement and impact on the global EWPD fit	26
3.1	Analysis setup	26
3.2	Extraction of the effective leptonic weak mixing angle	30
3.3	General SMEFT constraints	31
3.4	Constraints on lepton couplings	32
3.5	Constraints on quark couplings	34
A	Appendix: How to run the code	41

Introduction

The Standard Model (SM) of particle physics is an elegant, predictive, and very successful theory. However, it cannot explain certain phenomena, e.g., dark matter or neutrino masses, suggesting the existence of physics beyond the SM (BSM). One of the main goals of the LHC is to discover new particles and with them direct proof of BSM physics. So far this search has been unsuccessful, a likely explanation being that the energy required to produce them in sufficient numbers is beyond the reach of the LHC. However, it may be possible to observe new particles indirectly, as their existence will subtly influence the production of known particles at lower energies, resulting in systematic deviations from SM predictions.

The Standard Model Effective Field Theory (SMEFT [1, 2], see e.g. Ref. [3] for a comprehensive review) systematically parametrizes these potential deviations. It provides predictions for experimental observables in terms of an expansion in E/Λ and v/Λ , where E is the typical energy exchanged in the process, v the Higgs field’s vacuum expectation

value, and Λ the scale of BSM physics. This is achieved by extending the SM Lagrangian by a series of operators $\mathcal{O}_i^{(d)}$ that consist of gauge invariant combinations of SM fields with an energy dimension d greater than four:

$$\mathcal{L}_{\text{SMEFT}} = \mathcal{L}_{\text{SM}} + \sum_i \frac{c_i^{(5)}}{\Lambda} \mathcal{O}_i^{(5)} + \sum_i \frac{c_i^{(6)}}{\Lambda^2} \mathcal{O}_i^{(6)} + \dots \quad (0.1)$$

These operators are multiplied by dimensionless Wilson coefficients $c_i^{(d)}$, which are, along with Λ , the unknown parameters of the theory and reflect the strength of BSM interactions. At dimension-five there is only one type of operator, which violates lepton number conservation. The leading effects on collider physics observables are described by dimension-six operators, while the effect of operators of higher order are suppressed by increasing powers of $1/\Lambda$.

The measurement of electroweak precision observables (EWPOs), i.e., the Z pole observables precisely measured at LEP and SLD [4] as well as measurements of the W boson mass and partial widths, provide important constraints in the SMEFT. The high precision of measurements translates into stringent limits on Wilson coefficients. Since EWPO measurements involve relatively low energy scales E (compared to high-mass searches at the LHC), higher-order corrections in E/Λ to the observables are small. This makes the leading terms of the SMEFT expansion a good approximation of many BSM models. The inclusion of these tight and fairly model-independent constraints in any global SMEFT interpretation is thus crucial.

At the LHC, it is possible to further electroweak precision data (EWPD), for example by precisely measuring the effective leptonic weak mixing angle $\sin^2 \theta_{\text{eff}}^\ell$ or through the measurement of W boson properties, such as its mass, width, and branching fractions. In addition to advancing our knowledge of precision observables, the LHC allows for measurements of electroweak processes at high energies and studies of processes involving top quarks or Higgs bosons, potentially revealing anomalies that cannot be detected with EWPD alone. Understanding the existing constraints provided by precision data is crucial for appreciating the role of LHC measurements in constraining or discovering BSM physics within the SMEFT framework. It sharpens the focus of LHC data analysis on effects not already excluded by previous experiments.

To facilitate the combined analysis of LHC and electroweak precision data, a computer code that calculates the likelihood of Wilson coefficients based on precision measurements is presented in Section 1 of this paper. Section 2 discussed the impact of recent LHC measurements – of the W boson mass and width [5], the lepton flavour universality (LFU) of W branching fractions [6], and the effective leptonic weak mixing angle [7] – on this likelihood. It is demonstrated that the measurement of the effective leptonic weak mixing angle, which is based on the forward-backward asymmetry in Drell–Yan events, can be reinterpreted as one of the most precise LFU tests to date. To investigate the importance of forward–backward asymmetry measurements more thoroughly, an ATLAS Drell–Yan triple-differential cross-section measurement [8] is interpreted in a more general SMEFT framework in Section 3. This interpretation provides more accurate limits on

lepton couplings than the estimates obtained in the previous section and also constrains quark couplings.

1 An EWPD SMEFT likelihood for the LHC

The likelihood of electroweak precision data as a function of SMEFT Wilson coefficients, has been formulated in various ways in the literature [9–22]. This paper introduces a new `python` tool named `ewpd4lhc`¹ that is specifically designed for the combination with SMEFT interpretations of LHC data, like the ATLAS and CMS global EFT fits [23, 24]. The tool is easily configurable and returns numerical outputs in both text file format and as a `Roofit` [25] workspace, the latter being the primary format for combining likelihoods from the LHC experiments.

It provides SM and SMEFT predictions not only in the $\{\alpha, M_Z, G_\mu\}$ scheme used in most existing EWPD analyses but also in four alternative electroweak input parameter schemes, as listed in Table 1. Schemes using M_W as an input parameter, in particular the $\{M_W, M_Z, G_\mu\}$ scheme, are preferred for interpretations of LHC data [26].

SM predictions of observables in all schemes are dynamically calculated via interpolation formulas based on state-of-the-art theory predictions. The tool accurately models the correlated impact of input parameter uncertainties on SM predictions, which are substantial in schemes treating the less precisely known observables M_W or $\sin^2 \theta_{\text{eff}}^\ell$ as input parameters.

Baseline parametrizations are based on `SMEFTsim` [27, 28], with the option to include contributions quadratic in dimension-six Wilson coefficients, consistent with analyses from the ATLAS and CMS collaborations. Next-to-leading-order (NLO) perturbative [21, 29–32] corrections in the SMEFT as well as dimension-eight SMEFT contributions [20, 33] are available, too. Perturbative NLO corrections are in particular relevant for LHC analyses as large contributions from top quark operators arise at loop level, making EWPD constraints as important as measurements of top quark production at the LHC [34]. The three types of parametrizations are listed in Table 1, too. For all parametrizations, notations and operator definitions are in line `SMEFTsim` conventions.

SMEFT parametrizations included in the tool are compatible with the symmetry assumptions favoured for LHC analyses: fully flavour symmetric scenarios as well as the $U(2)_q \times U(2)_u \times U(2)_d$ scenario for top physics [35], both with and without lepton flavour universality assumption. Available symmetry assumptions are also listed in Table 1.

Section 1.1 introduces precision W and Z pole observables in `ewpd4lhc` and their prediction in the SM is described in Section 1.2. The modelling of the effect of uncertainties in input parameters as well as theory uncertainties is discussed in Section 1.3. The implementation of the uncertainty model is validated by performing an electroweak fit described in Section 1.4. Section 1.5 outlines the derivation of SMEFT corrections to the SM predictions and a fit of EWPD in the SMEFT is presented in Section 1.6.

¹Available at <https://github.com/ewpd4lhc/ewpd4lhc>

<code>ewpd41hc</code> option	Internal notation	Explanation
Input scheme	<code>alpha</code>	$\{\alpha, M_Z, G_\mu\}$
	<code>MW</code>	$\{M_W, M_Z, G_\mu\}$
	<code>alphaMW</code>	$\{\alpha, M_W, M_Z\}$
	<code>sin2theta</code>	$\{\sin^2 \theta_{\text{eff}}^\ell, M_Z, G_\mu\}$
	<code>alphasin2theta</code>	$\{\alpha, \sin^2 \theta_{\text{eff}}^\ell, M_Z\}$
Parametrizations	<code>SMEFTsim</code>	Linear and quadr. dim.-six dependence [28]
	<code>EWPDatNLO</code>	Linear and quadr. dim.-six dependence, NLO [32]
	<code>EWP2dim8</code>	Full $O(\Lambda^{-4})$ dependence, incl dim. eight [20]
Symmetries	<code>general</code>	General but massless light quarks, diag. CKM
	<code>top</code>	$U(2)_q \times U(2)_u \times U(2)_d$
	<code>topU3l</code>	$U(2)_q \times U(2)_u \times U(2)_d \times U(3)_l \times U(3)_e$
	<code>U35</code>	$U(3)_q \times U(3)_u \times U(3)_d \times U(3)_l \times U(3)_e$

Table 1. Electroweak input parameter schemes, SMEFT parametrizations, and symmetry assumptions included in `ewpd41hc`. The electroweak parameters are the fine-structure constant α , the W and Z boson masses, M_W and M_Z , the Fermi constant from muon decays, G_μ , and the effective weak mixing angle, $\sin^2 \theta_{\text{eff}}^\ell$. The symmetry assumptions are described in detail in Ref. [28].

1.1 Input observables

The `ewpd41hc` code incorporates observables sensitive to couplings of the Z and W boson to all lepton flavours, charm quarks, and bottom quarks. It also considers the total width and hadronic branching fractions of the W and Z bosons, which constrain combinations of fermion couplings. However, observables that distinguish the three lightest quark flavours are not included due to insufficient measurement precision. Measurements of $\sin^2 \theta_{\text{eff}}^\ell$ derived from the charge asymmetry Q_{FB}^{had} at LEP and the forward–backward asymmetry at hadron colliders, A_{FB} , are also not considered due to their model-dependent extraction, requiring for example SM-like quark couplings. A more accurate interpretation of this type of measurement is discussed in Section 3.

The (pseudo) observables Γ_Z , σ_{had}^0 , R_ℓ (replaced by R_e , R_μ , and R_τ in SMEFT scenarios without LFU), R_c , and R_b , constrain combinations of Z boson partial widths:

$$\sigma_{\text{had}}^0 = \frac{12\pi}{M_Z^2} \frac{\Gamma_{Z \rightarrow e^+e^-} \Gamma_{Z \rightarrow \text{had}}}{\Gamma_Z^2}, \quad R_\ell = \frac{\Gamma_{Z \rightarrow \text{had}}}{\Gamma_{Z \rightarrow \ell^+ \ell^-}}, \quad R_b = \frac{\Gamma_{Z \rightarrow b\bar{b}}}{\Gamma_{Z \rightarrow \text{had}}}, \quad R_c = \frac{\Gamma_{Z \rightarrow c\bar{c}}}{\Gamma_{Z \rightarrow \text{had}}}. \quad (1.1)$$

They are sensitive to the combined effect of the Z boson couplings to left-handed and right-handed fermions (or equivalently, vector and axial vector couplings) and have been precisely measured at LEP and SLD [4]. The values used in `ewpd41hc` include an updated estimate of the LEP luminosity [36], as recommended by the particle data group (PDG) [37].

The results of asymmetry measurements utilizing the polarized beams of SLC — A_ℓ^{SLD} (A_e^{SLD} , A_μ^{SLD} , and A_τ^{SLD} if not assuming LFU), A_c , and A_b — as well as τ polarization measurements at LEP, A_ℓ^{LEP} (A_e^{LEP} and A_τ^{LEP}), are also included for both lepton flavour universal and non-universal cases. These measurements allow distinguishing couplings of

left-handed and right-handed fermions, as the following relationship holds:

$$A_f = \frac{\Gamma_{Z \rightarrow f_L \bar{f}_L} - \Gamma_{Z \rightarrow f_R \bar{f}_R}}{\Gamma_{Z \rightarrow f \bar{f}}}. \quad (1.2)$$

The forward–backward asymmetries on the Z peak measured by LEP, $A_{\text{FB}}^{0,\ell}$ ($A_{\text{FB}}^{0,e}$, $A_{\text{FB}}^{0,\mu}$, and $A_{\text{FB}}^{0,\tau}$ without LFU), $A_{\text{FB}}^{0,c}$, and $A_{\text{FB}}^{0,b}$ also serve this purpose. They are related to the asymmetry parameters A_f by:

$$A_{\text{FB}}^{0,f} = \frac{3}{4} A_f A_e. \quad (1.3)$$

The PDG values of W boson branching fractions, B_W^{had} , (B_W^e , B_W^μ , and B_W^τ if not assuming LFU), based on LEP, and the total width, derived from a LEP+Tevatron combination, Γ_W , are used to constrain the W couplings to (left-handed) fermions. An LHC average for ratios of W branching fractions,

$$R_W^{\mu/e} = \frac{B_W^\mu}{B_W^e}, \quad R_W^{\tau/e} = \frac{B_W^\tau}{B_W^e}, \quad R_W^{\tau/\mu} = \frac{B_W^\tau}{B_W^\mu}, \quad (1.4)$$

which excludes contributions from LEP (and Tevatron) data but is based on ATLAS [38, 39], CMS [40], and LHCb [41] measurements, is also included. The role of the latest ATLAS measurement of LFU in W boson decays [6] is more subtle and discussed in Section 2.

To predict these observables in the SM, knowledge of three electroweak input parameters is required, usually taken to be three of the set $\{\alpha, G_\mu, M_W, M_Z, \sin^2 \theta_{\text{eff}}^\ell\}$. They enable the calculation of all other electroweak parameters. In the SMEFT, the remaining parameters are not solely determined by the SM input parameter values but also depend on Wilson coefficients. Like any other observable, their measurement can thus provide constraints on BSM physics. PDG values are used for M_W (which currently excludes the CDF result [42] and does not yet incorporate the preliminary CMS result [43]), M_Z , the Fermi coupling determined from muon decays, G_μ , and the fine-structure constant $\alpha(Q^2=0)$.

While the electromagnetic coupling at low scales, $\alpha(Q^2=0)$, is known precisely, it is the electromagnetic coupling at the Z boson energy scale, $\alpha(Q^2 = M_Z^2)$, that is required for the prediction of W and Z pole observables, including M_W . The running of the coupling up to $Q^2 = M_Z^2$ cannot be reliably calculated using perturbative QCD alone, due to the existence of hadronic resonances in the intermediate Q^2 region. Instead, $\Delta\alpha = 1 - \frac{\alpha(Q^2=0)}{\alpha(Q^2=M_Z^2)}$ is typically determined using additional experimental inputs. By default `ewpd41hc` uses the value of Ref. [44] in combination with the theoretical calculation of the leptonic contributions [45]. In schemes using M_W or $\sin^2 \theta_{\text{eff}}^\ell$ instead of α as an input, $\alpha(Q^2 = M_Z^2)$ is predicted by the SM. In that case `ewpd41hc` treats $\Delta\alpha$ — implicitly combined with $\alpha(Q^2=0)$, which carries negligible uncertainty — as an observable. This approach has recently been explored in Ref. [46], too, albeit missing the parametric uncertainty discussed below. An alternative approach, used in [47], involves using the value of $\alpha(Q^2 = M_Z^2)$ implied by Bhabha scattering measurements at LEP, although these measurements are less precise and introduce additional dependences on four-fermion operators in the SMEFT.

If $\sin^2 \theta_{\text{eff}}^\ell$ is taken as a SM input, its value is automatically determined in a fit of all observables that depend on $\sin^2 \theta_{\text{eff}}^\ell$ but do not carry additional Wilson coefficient dependence, i.e., A_ℓ^{SLD} , A_ℓ^{LEP} and $A_{\text{FB}}^{0,\ell}$. Observables that depend on additional couplings, like

$A_{\text{FB}}^{0,b}$, are not considered at that stage. If LFU is not assumed, the input parameter is the effective weak mixing angle for electrons, $\sin^2 \theta_{\text{eff}}^e$, determined by A_e^{SLD} , A_e^{LEP} , and $A_{\text{FB}}^{0,e}$.

The strong coupling α_s , also needed for the prediction of precision observables, is set to the average of the Flavour Lattice Averaging Group (FLAG) [48], rather than the PDG value, as the lattice extraction is more robust against SMEFT effects [49].

The Higgs boson and top quark masses, M_H and m_t , contribute to SM predictions of EWPOs at loop level. The values used in `ewpd41hc` correspond to the PDG average, with an additional 0.5 GeV uncertainty on m_t , to account for ambiguities in the top mass definition [50].

Correlations in the measurements of $\{M_Z, \Gamma_Z, \sigma_{\text{had}}^0, R_\ell, A_{\text{FB}}^{0,\ell}\}$ (or their counterparts without assuming LFU), $\{A_e^{\text{SLD}}, A_\mu^{\text{SLD}}, A_\tau^{\text{SLD}}\}$, $\{A_e^{\text{LEP}}, A_\tau^{\text{LEP}}\}$, $\{R_b, R_c, A_{\text{FB}}^{0,b}, A_{\text{FB}}^{0,c}, A_b, A_c\}$, and $\{B_W^e, B_W^\mu, B_W^\tau\}$, are taken into account within each group indicated by braces.

The `ewpd41hc` enables users to transparently set the measured values of observables, including SM input parameters, and their correlation in a `yaml` text file. A subset of observables can be chosen in the main configuration file of the tool. The default central values can be found in Table 2 (Table 5) assuming (not assuming) LFU, alongside the fit results discussed in the following sections.

1.2 SM predictions

Precise SM predictions for the above observables are calculated, typically with at least two-loop accuracy, using interpolation formulas. These predictions are later combined with lower-accuracy predictions of the Wilson-coefficient dependent corrections within the SMEFT framework.

Central predictions for $R_\ell, R_c, R_b, \sin^2 \theta_{\text{eff}}^\ell$, and $\sin^2 \theta_{\text{eff}}^b$ are calculated from the SM input observables M_Z, M_H, m_t, α_s , and $\Delta\alpha$, using the formulas of Ref. [51]. A correction that accounts for the small impact of G_μ variations is implemented at one-loop level. For $\sin^2 \theta_{\text{eff}}^c$ the formulas of Ref [52] are used. The effective weak mixing angles $\sin^2 \theta_{\text{eff}}^\ell$ as well as $\sin^2 \theta_{\text{eff}}^b$ and $\sin^2 \theta_{\text{eff}}^c$ determine the values of $A_\ell, A_{\text{FB}}^{0,\ell}, A_b, A_c, A_{\text{FB}}^{0,c}$, and $A_{\text{FB}}^{0,b}$, using

$$A_f = \frac{1 - 4|Q_f| \sin^2 \theta_{\text{eff}}^f}{1 - 4|Q_f| \sin^2 \theta_{\text{eff}}^f + 8(Q_f \sin^2 \theta_{\text{eff}}^f)^2} \quad (1.5)$$

and Equation 1.3. The W boson mass is predicted as per Ref. [53] while a one-loop prediction for the width Γ_W is taken from [54].

To obtain predictions using the four alternative input parameter sets listed in Table 1, either α or G_μ is substituted for M_W or $\sin^2 \theta_{\text{eff}}^\ell$ as inputs to the interpolation formulas, following the methodology of Ref. [47]. Although these predictions still rely on the $\{\alpha, M_Z, G_\mu\}$ scheme for SM calculations, this approach enables the use of different input parameter sets for SMEFT analyses, where alternative configurations provide advantages [26]. For instance, to calculate predictions using the set of $\{M_W, M_Z, G_\mu\}$, the relationship $M_W(\Delta\alpha, \dots)$ given in Ref. [53] is inverted to obtain $\Delta\alpha(M_W, \dots)$, which is subsequently substituted into the interpolation formulas. Similarly, the inversion of the $M_W - G_\mu, \sin^2 \theta_{\text{eff}}^\ell - \alpha$, or $\sin^2 \theta_{\text{eff}}^\ell - G_\mu$ relationships enables the code to provide predictions in the remaining three schemes of Table 1.

1.3 Treatment of uncertainties

The `ewpd4lhc` model of the likelihood L is based on a multivariate Gaussian distribution,

$$-2 \log L = \chi^2 = (\Delta \mathbf{x}^\top V^{-1} \Delta \mathbf{x}), \quad (1.6)$$

where

$$\Delta \mathbf{x} = \mathbf{x}_{\text{meas}} - \mathbf{x}_{\text{pred}} \quad (1.7)$$

represents the difference between the measured values \mathbf{x}_{meas} and predicted values \mathbf{x}_{pred} of observables. The prediction is a combination of the SM prediction $\mathbf{x}_{\text{pred}}^{\text{SM}}$ and Wilson-coefficient-dependent SMEFT corrections. The covariance matrix V encodes uncertainties.

Uncertainties arise not only in the measurement of observable but also in their prediction. These include ‘‘parametric uncertainties’’ in the SM prediction, which stem from uncertainties in input parameters, as well as ‘‘theory uncertainties’’, which arise for example due to missing higher-order corrections in theoretical calculations.

The `ewpd4lhc` tool provides two options to account for parametric uncertainties. The default method is to include their effect in the covariance V , along with the uncertainty of measurements. In this approach SM predictions $\mathbf{x}_{\text{pred}}^{\text{SM}}$ are fixed to the values implied by the nominal input parameter values, $\mathbf{x}_{\text{meas}}^{\text{in}}$. The alternative is to model the dependence of $\mathbf{x}_{\text{pred}}^{\text{SM}}$ on SM input parameters with nuisance parameters \mathbf{x}^{in} that are part of the likelihood, so that $\mathbf{x}_{\text{pred}}^{\text{SM}} \equiv \mathbf{x}_{\text{pred}}^{\text{SM}}(\mathbf{x}^{\text{in}})$.

In the input-parameter-free likelihood approach, the the method most commonly used in analyses of EWPD to date, the difference between measurement and SM prediction, $\Delta \mathbf{x}^{\text{SM}} = \mathbf{x}_{\text{meas}} - \mathbf{x}_{\text{pred}}^{\text{SM}}$, is treated as the random variable within the multivariate Gaussian model. In this framework, parametric uncertainties of $\mathbf{x}_{\text{pred}}^{\text{SM}}$ must be incorporated into the covariance matrix V . This becomes particularly important when M_W or $\sin^2 \theta_{\text{eff}}^\ell$ are treated as input parameters, as the parametric uncertainty in the prediction of some observables can then become similar to or even greater than the uncertainty associated with the direct measurements.

The impact of this parametric uncertainties on the prediction of EWPOs is highly correlated. To illustrate the extent of this correlation, one million pseudo data sets were generated. These sets include $\Delta\alpha$, Z pole observables, as well as the SM inputs, taken to be $\{M_W, M_Z, G_\mu\}$, were sampled randomly according to their experimental covariance. SM predictions for each pseudo data set were calculated using the formulas introduced in Section 1.2. Figure 1 presents the sample correlation coefficient for measurements \mathbf{x}_{meas} and the difference between measurement and prediction, $\Delta \mathbf{x}^{\text{SM}} = \mathbf{x}_{\text{meas}} - \mathbf{x}_{\text{pred}}^{\text{SM}}$. The correlation of uncertainties in $\Delta \mathbf{x}^{\text{SM}}$ is significantly higher than that of the measured values \mathbf{x}_{meas} alone, highlighting the importance of an accurate correlation model.

The `ewpd4lhc` code employs linear error propagation to construct the covariance matrix rather than relying on the pseudo experiments used to generate Figure 1. The contribution to the covariance from parametric uncertainties, V^{param} , is calculated as

$$V_{ij}^{\text{param}} = \sum_k \frac{\partial x_{\text{pred},i}^{\text{SM}}}{\partial x_k^{\text{in}}} \Big|_{x_k^{\text{in}}=x_{\text{meas},k}^{\text{in}}} \times \frac{\partial x_{\text{pred},j}^{\text{SM}}}{\partial x_k^{\text{in}}} \Big|_{x_k^{\text{in}}=x_{\text{meas},k}^{\text{in}}} \times \sigma_{\text{meas},k}^2. \quad (1.8)$$

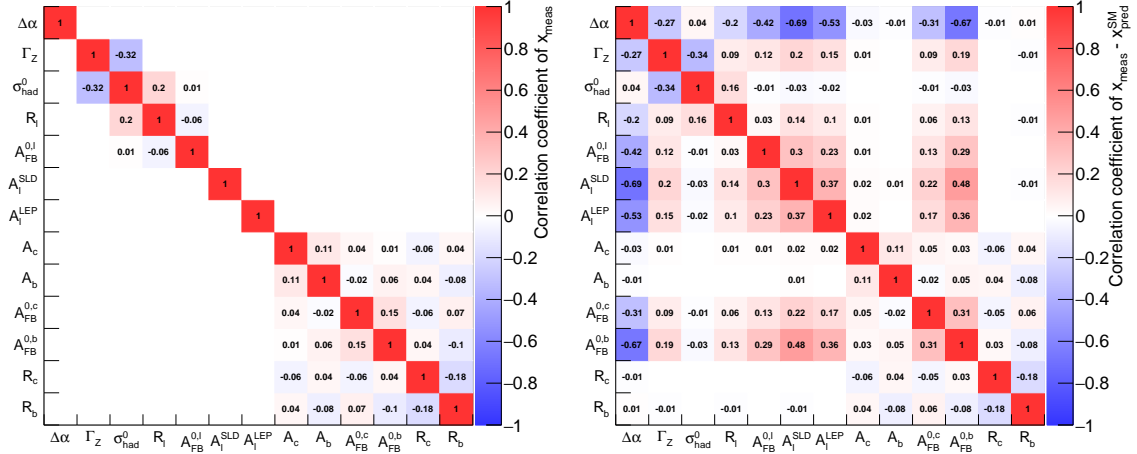


Figure 1. Comparison of the correlation coefficient of various Z -pole measurements and $\Delta\alpha$ (left) with the correlation coefficient of the difference of measurement and SM prediction, $\Delta\mathbf{x}^{\text{SM}} = \mathbf{x}_{\text{meas}} - \mathbf{x}_{\text{pred}}^{\text{SM}}$, in the $\{M_W, M_Z, G_\mu\}$ input parameter scheme (right). The latter is particularly important in the SMEFT analysis, where differences between measurement and prediction may indicate potential signs of BSM physics.

Here, $\sigma_{\text{meas},k}$ represents the uncertainty in the measured value $x_{\text{meas}}^{\text{in}}$. The Jacobian matrix $\frac{\partial \mathbf{x}_{\text{pred}}^{\text{SM}}}{\partial \mathbf{x}^{\text{in}}}$, which is implemented in `ewpd41hc` for all input parameters schemes offered, is evaluated dynamically based on the provided measurement values. The analytically derived covariance shows excellent agreement with the one in Figure 1, confirming the correct technical implementation and indicating that the impact of uncertainty propagation beyond the linear contribution is negligible.

As an alternative to the nuisance-parameter-free scheme, the likelihood of Equation 1.6 can be formulated to include the SM input observables, \mathbf{x}^{in} , in the observables \mathbf{x} explicitly considered in the multivariate Gaussian model. In that case, \mathbf{x}_{pred} of Equation 1.7 is a function of both SM parameters and Wilson coefficients, where this dependence is trivial for SM input parameters: $\mathbf{x}_{\text{pred}}^{\text{in}} = \mathbf{x}^{\text{in}}$. In this alternative approach the random variable of the multivariate Gaussian is \mathbf{x}_{meas} , not the difference between measurement and SM prediction $\Delta\mathbf{x}^{\text{SM}}$. Given that the linear approximation provides a sufficiently accurate model of uncertainties, a linear version of the full interpolation formulas for SM predictions is implemented, also utilizing the Jacobian matrix $\frac{\partial \mathbf{x}_{\text{pred}}^{\text{SM}}}{\partial \mathbf{x}^{\text{in}}}$:

$$\mathbf{x}_{\text{pred}}^{\text{SM}}(\mathbf{x}_{\text{in}}) = \mathbf{x}_{\text{pred}}^{\text{SM}}(\mathbf{x}_{\text{in}}^{\text{meas}}) + (\mathbf{x}_{\text{in}} - \mathbf{x}_{\text{in}}^{\text{meas}}) \frac{\partial \mathbf{x}_{\text{pred}}^{\text{SM}}}{\partial \mathbf{x}_{\text{in}}} \Big|_{\mathbf{x}_{\text{in}} = \mathbf{x}_{\text{in}}^{\text{meas}}}. \quad (1.9)$$

The linearized formula simplifies the SM fit and enables a stable, efficient combined fit of SM parameters and Wilson coefficients in the SMEFT. The validity of the linear approximation is confirmed by comparison with the full interpolation formulas, with two examples illustrating relatively large (yet still negligible) non-linear contributions shown in Figure 2. Indeed, when the inputs to the interpolation formulas are varied within three standard deviations of their measured values, only the α_s and $\sin^2 \theta_{\text{eff}}^\ell$ dependence in certain predictions

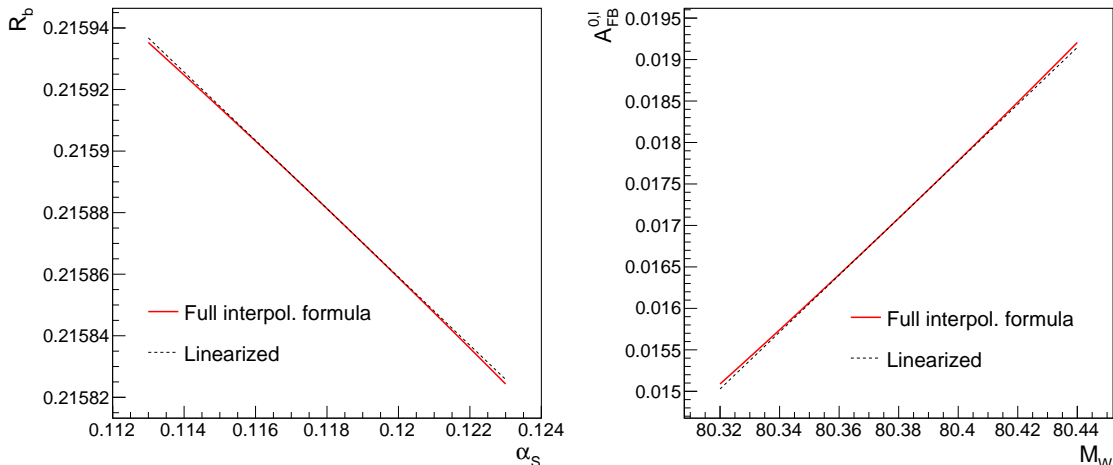


Figure 2. Examples of the dependence of EWPO predictions on experimental inputs. The plots show R_b (left) and $A_{\text{FB}}^{0,\ell}$ (right) as functions of the inputs α_s and M_W , respectively, using the full interpolation formulas from Ref. [51] and their linear approximation around the central prediction, as implemented in the code presented in this paper. The inputs quantities α_s and M_W are varied by about five standard deviations around the values determined from direct measurements.

deviates by more than 2% from the linear approximation. The impact of α_s variations on the SMEFT fit is minimal, and the non-linear dependence on $\sin^2 \theta_{\text{eff}}^\ell$ is significant only when $\sin^2 \theta_{\text{eff}}^\ell$ is treated as an input parameter.

As with parametric uncertainties, two options are provided for addressing theory uncertainties. They can either be added directly to the covariance matrix or be incorporated in the parametrization, in which case Gaussian constraint terms are added for each nuisance parameter to the likelihood. Theoretical uncertainties are accounted for in M_W (4 MeV, from Ref. [53]), R_ℓ , R_c , R_b , and $\sin^2 \theta_{\text{eff}}^\ell$ (see Ref. [51]). The uncertainties in $\sin^2 \theta_{\text{eff}}^b$ and $\sin^2 \theta_{\text{eff}}^c$ prediction are negligible compared to the experimental precision of measurements. There is no theory uncertainty for M_W or $\sin^2 \theta_{\text{eff}}^\ell$ if used as input. Instead the replaced input parameters $\Delta\alpha$ or G_μ have uncertainty of $\sigma_{\text{old inp.}}^{\text{theo}} = \frac{\partial x_{\text{old inp.}}}{\partial x_{\text{new inp.}}} \sigma_{\text{new inp.}}^{\text{theo}}$, where $\sigma_{\text{new inp.}}^{\text{theo}}$ is the M_W or $\sin^2 \theta_{\text{eff}}^\ell$ theory uncertainty in the original $\{\alpha, M_Z, G_\mu\}$ scheme calculation.

1.4 The EWPD fit in the SM

The linear parametrization of SM relations (Equation 1.9) enables the algebraic minimization of Equation 1.6, thus solving the SM fit. This fit is performed automatically when running the `ewpd4lhc` code. Free parameters of the fit are M_Z , M_H , m_t , α_s , and — depending on the electroweak input parameter scheme chosen — two of $\Delta\alpha$, M_W , G_μ , $\sin^2 \theta_{\text{eff}}^\ell$, as well as nuisance parameters modelling theory uncertainties. The results of fits using different input parameter sets show only marginal differences, due to the differing role of the theoretical uncertainties on M_W and $\sin^2 \theta_{\text{eff}}^\ell$.

Fit results for the default configuration and using $\Delta\alpha$ and G_μ as input, are presented in

Observable	Direct	Fit	Pull	Indirect
M_H [GeV]	125.20 ± 0.11	125.20 ± 0.11	-0.0	106 ± 27
m_t [GeV]	172.57 ± 0.58	172.68 ± 0.56	0.2	174.2 ± 2.2
α_s	0.11840 ± 0.00080	0.11854 ± 0.00077	0.2	0.1202 ± 0.0028
$\Delta\alpha$	0.05903 ± 0.00010	0.05902 ± 0.00010	-0.1	0.05886 ± 0.00042
G_μ [10^{-5}GeV^{-2}]	1.1663788 ± 0.0000006	1.1663788 ± 0.0000006	0.0	1.16658 ± 0.00044
M_Z [GeV]	91.1875 ± 0.0021	91.1877 ± 0.0020	0.1	91.1960 ± 0.0095
M_W [GeV]	80.369 ± 0.013	80.358 ± 0.006	-0.8	80.356 ± 0.006
Γ_Z [GeV]	2.4955 ± 0.0023	2.4947 ± 0.0006	-0.3	2.4947 ± 0.0006
R_ℓ	20.767 ± 0.025	20.754 ± 0.007	-0.5	20.752 ± 0.008
R_c	0.1721 ± 0.0030	0.1722 ± 0.0001	0.0	0.1722 ± 0.0001
R_b	0.21629 ± 0.00066	0.21587 ± 0.00010	-0.6	0.21587 ± 0.00010
σ_{had}^0 [pb]	41480 ± 32	41488 ± 7	0.2	41489 ± 7
A_ℓ^{SLD}	0.1513 ± 0.0021	0.1475 ± 0.0004	-1.8	0.1474 ± 0.0005
A_ℓ^{LEP}	0.1465 ± 0.0033	0.1475 ± 0.0004	0.3	0.1476 ± 0.0005
$A_{\text{FB}}^{0,\ell}$	0.0171 ± 0.0010	0.0163 ± 0.0001	-0.8	0.0163 ± 0.0001
$A_{\text{FB}}^{0,b}$	0.0992 ± 0.0016	0.1031 ± 0.0003	2.4	0.1033 ± 0.0003
$A_{\text{FB}}^{0,c}$	0.0707 ± 0.0035	0.0737 ± 0.0002	0.9	0.0737 ± 0.0002
A_b	0.923 ± 0.020	0.935 ± 0.000	0.6	0.935 ± 0.000
A_c	0.670 ± 0.027	0.668 ± 0.000	-0.1	0.668 ± 0.000
Γ_W [GeV]	2.085 ± 0.042	2.090 ± 0.000	0.1	2.090 ± 0.000
B_W^{had}	0.6741 ± 0.0027	0.6754 ± 0.0000	0.5	0.6754 ± 0.0000

Table 2. Input values and fit results for the SM fit of the first six observables in the table. Uncertainties on the remaining observables are obtained via error propagation. Pull values are calculated as the difference of fit result and direct measurement, divided by the uncertainty of the direct measurement. The column labeled “indirect” contains the result of a fit that does not include the direct measurement corresponding to each respective row.

Table 2. The only significant deviations of direct measurements from the global fit results are the well-known tensions in $A_{\text{FB}}^{0,b}$ and A_ℓ^{SLD} measurements.

The results are in good agreement with established codes for the SM fit. For instance, the latest **Gfitter** result [55] predicts $\alpha_s = 0.1198 \pm 0.0029$, in good agreement with this result, $\alpha_s = 0.1202 \pm 0.0028$. Half of the 2 MeV difference to the indirect **Gfitter** W mass prediction, $M_W = 80354 \pm 7$ MeV, can be attributed to a different value for $\Delta\alpha$. The **Gfitter** Higgs mass $M_H = 100_{-21}^{+25}$ GeV, has slightly smaller uncertainties than presented here, mainly because non-linear effects in the M_H predictions become important when the direct M_H constrained is ignored. The exact cause for the one GeV difference to the top mass prediction by **Gfitter**, $m_t = 175.15_{-2.39}^{+2.37}$ GeV could not be identified, part of it is related to the small differences observed for M_W .

The indirect prediction of SM parameters (which have all been precisely measured for more than a decade) is not the main use case of this tool, which is designed to facilitate accurate SMEFT fits. The good agreement with more sophisticated tools still demonstrates that it can also be useful for the calculation of SM predictions and to obtain instant results of the electroweak fit.

1.5 SMEFT parametrization

Predictions in the SM are extended by a parametrization of the effect of higher-dimensional operators, to obtain predictions in the SMEFT framework. The SMEFT contributions to EWPOs can be described, at leading order, by 10 to 23 dimension-six Wilson coefficients, depending on symmetry assumptions. There are no contributions of dimension-five or dimension-seven operators and higher orders are strongly suppressed. At next-to-leading order 35 (more than 100) operators contribute in the flavour universal (general) case, although the contribution of most of the extra operators, contributing at loop-level, is relatively small.

The predicted values of observables, $x_{\text{pred},i}$, can be decomposed into the SM prediction, $x_{\text{pred},i}^{\text{SM}}$, and a SMEFT correction, $\Delta_{\text{SMEFT},i}$, that depends on Wilson coefficients:

$$x_{\text{pred},i} = x_{\text{pred},i}^{\text{SM}} + \Delta_{\text{SMEFT},i} = x_{\text{pred},i}^{\text{SM}} + \sum_j A_{ij}^{(6)} \frac{c_j^{(6)}}{\Lambda^2} + \sum_{j,k} B_{ijk}^{(6)} \frac{c_j^{(6)} c_k^{(6)}}{\Lambda^4} + \sum_j A_{ij}^{(8)} \frac{c_j^{(8)}}{\Lambda^4} + \dots \quad (1.10)$$

Here, $A_{ij}^{(6)}$ and $\sum_{j,k} B_{ijk}^{(6)}$ are a real-valued matrix and a tensor that parametrize the linear and quadratic dependence on dimension-six Wilson coefficients, while $A_{ij}^{(8)}$ parametrizes the linear dependence on dimension-eight operators. The linear dependence on dimension-six Wilson coefficients, arising from the interference of amplitudes with dimension-six operator insertions with the SM, is expected to be the most important contribution, as it is the leading term in the $1/\Lambda$ expansion.

EWPD typically constrains deviations from the SM to be at most a few percent, making it crucial to consider percent-level higher-order corrections to SM predictions, as well as the precise input parameter dependence of $\mathbf{x}_{\text{pred}}^{\text{SM}}$. They can introduce percent-level corrections to the SM and thus $O(1)$ effects on Wilson coefficient constraints. In contrast, percent-level corrections to Δ_{SMEFT} will affect results typically at the same order of magnitude. Therefore, a leading order parametrization of SMEFT effects is often sufficient, and the input parameter dependence of Δ_{SMEFT} is neglected in `ewpd4lhc`, which uses fixed parametrizations stored in `yaml` text files.

Baseline dimension-six parametrizations of the SMEFT correction have been derived with the `SMEFTsim` [28] model at leading order. First, linear and quadratic parametrizations of the partial widths for all W decays and polarized Z decays are obtained by simulating the boson decays in `MadGraph5_aMC@NLO` [56, 57], with negligible numerical uncertainties. Fermions except for the top and bottom quarks are considered massless, as is usually the assumption in LHC studies. In a second step, parametrizations of EWPOs are calculated as sums, differences, products or ratios of (polarized) partial widths and expanded to second order in the Wilson coefficients. The Wilson-coefficient dependent shifts of M_W or α are extracted directly from the UFO model. The linear dependence of the W width on Wilson coefficients affecting the W mass is taken into account following Ref. [58]. Parametrizations are provided for two input parameter schemes and for the $U(2)_q \times U(2)_u \times U(2)_d$ (referred to as `top` in `SMEFTsim`), $U(2)_q \times U(2)_u \times U(2)_d \times U(3)_\ell \times U(3)_e$ (`topU31`), and $U(3)_q \times U(3)_u \times U(3)_d \times U(3)_\ell \times U(3)_e$ (`U35`), and general SMEFT symmetry assumptions. The advantage of

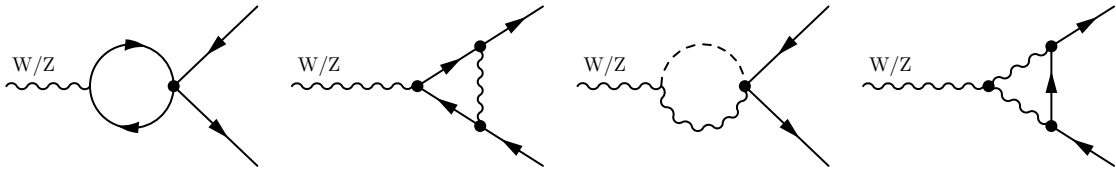


Figure 3. Examples of next-to-leading order Feynman diagrams for W and Z boson decays in the SMEFT. Possible insertions of dimension-six operators are marked with dots.

this approach is that it ensures parametrizations are consistent with those used at the LHC, which either use `SMEFTsim` or models that have been validated against it [59]. This method also includes contributions quadratic in dimension-six Wilson coefficients, analogous to the approach used in LHC analyses. The code allowing for the derivation of parametrizations is included in `ewpd4lhc`, allowing users to re-derive them with different input values or, with minor modifications, to use alternative EFT scenarios.

Two types of higher-order corrections to the SMEFT parametrizations are included in `ewpd4lhc` as alternative parametrization that can also be used in combination.

Next-to-leading-order QCD and EW perturbative corrections [21, 29–32] modify tree-level parametrizations by a few percent and introduce new dimension-six Wilson coefficients that only emerge at the loop level (example Feynman diagrams are shown in Figure 3). These corrections have recently [31, 32] been computed in the flavour-general case and for all five input parameter schemes listed in Table 1. Analytic expressions, kindly provided by the authors of Ref. [32], are available as ancillary files accompanying the corresponding arXiv submission. Numerical implementations of these corrections have been incorporated in `ewpd4lhc`, using electroweak input parameter values aligned with the `SMEFTsim` defaults. Expressions for a broader set of derived observables and under various symmetry assumptions are also made available in `ewpd4lhc`. The NLO parametrizations were cross-validated against the numerical results in Ref. [21]. Observed differences, at the 10% level, are consistent with variations in input parameter values, particularly the choice of α .

Also available, in the $\{\alpha, M_Z, G_\mu\}$ and $\{M_W, M_Z, G_\mu\}$ input parameter schemes and currently only for Z pole observables, are the complete Λ^{-4} [20, 33, 60] corrections, which modify the dependence on dimension-six squared contributions and introduce a new linear dependence on dimension-eight operators. They have also been adapted to the flavour symmetries mentioned above.

The three parametrizations from `SMEFTsim`, Ref. [20] (labeled `EWPD2dim8`), and those based on Ref. [32] (labeled `EWPDatNLO` and `EWPDatLO` for the NLO and LO case) have been compared to ensure consistency of the initial parametrizations and correctness of the conversion to various flavour symmetries. The comparison of the coefficients of the parametrizations for A_ℓ is shown in Table 3, for the fully flavour symmetric case and the $\{M_W, M_Z, G_\mu\}$ input parameter scheme. The operator definitions and notations from Ref. [28] are used for Warsaw basis [2] Wilson coefficients throughout this paper while the notation of Ref. [20] is used from dimension-eight Wilson coefficients. At leading order, differences between the parametrizations are less than 5% for all observables and are mainly

δA_ℓ	Wilson coef.	SMEFTsim	EWPD2dim8	EWPDatLO	EWPDatNLO
Dim-6	c_{HWB}	0.195	0.192	0.195	0.212
$O(\Lambda^2)$	c_{HD}	0.182	0.179	0.182	0.196
	$c_{HI}^{(1)}$	0.104	0.102	0.104	0.115
	$c_{HI}^{(3)}$	0.104	0.102	0.104	0.122
	c_{He}	0.13	0.127	0.13	0.132
	$c_{Hq}^{(1)}$	—	—	—	0.013
	$c_{Hq}^{(3)}$	—	—	—	-0.008
	c_{Hu}	—	—	—	-0.017
	c_W	—	—	—	-0.001
	c_{uB}	—	—	—	-0.003
	c_{uW}	—	—	—	0.002
	$c_{lq}^{(1)}$	—	—	—	0.002
	$c_{lq}^{(3)}$	—	—	—	-0.003
	c_{lu}	—	—	—	-0.003
	c_{qe}	—	—	—	0.002
	c_{eu}	—	—	—	-0.003
Dim-6	$c_{HWB} c_{HWB}$	-0.006	-0.007	—	—
$O(\Lambda^4)$	$c_{HWB} c_{HI}^{(1)}$	-0.019	-0.018	—	—
	$c_{HWB} c_{HI}^{(3)}$	-0.007	-0.018	—	—
	$c_{HWB} c_{He}$	0.003	0.003	—	—
	$c_{HWB} c_{ll}^{(1)}$	-0.006	0.0	—	—
	$c_{HD} c_{HWB}$	-0.009	-0.019	—	—
	$c_{HD} c_{HD}$	-0.003	-0.006	—	—
	$c_{HD} c_{HI}^{(1)}$	-0.016	-0.017	—	—
	$c_{HD} c_{HI}^{(3)}$	-0.005	-0.017	—	—
	$c_{HD} c_{He}$	0.005	0.003	—	—
	$c_{HD} c_{ll}^{(1)}$	-0.006	0.0	—	—
	$c_{HI}^{(1)} c_{HI}^{(1)}$	-0.008	-0.008	—	—
	$c_{HI}^{(1)} c_{HI}^{(3)}$	-0.01	-0.016	—	—
	$c_{HI}^{(1)} c_{ll}^{(1)}$	-0.003	-0.0	—	—
	$c_{HI}^{(3)} c_{HI}^{(3)}$	-0.002	-0.008	—	—
	$c_{HI}^{(3)} c_{ll}^{(1)}$	-0.003	-0.0	—	—
	$c_{He} c_{HI}^{(1)}$	-0.006	-0.006	—	—
	$c_{He} c_{HI}^{(3)}$	0.002	-0.006	—	—
	$c_{He} c_{He}$	0.005	0.005	—	—
	$c_{He} c_{ll}^{(1)}$	-0.004	-0.0	—	—
	$c_{HB} c_{HWB}$	—	0.012	—	—
	$c_{HW} c_{HWB}$	—	0.012	—	—
Dim-8	$c_{HWB}^{(8)}$	—	0.006	—	—
$O(\Lambda^4)$	$c_{HDD,2}^{(8)}$	—	0.011	—	—
	$c_{HI}^{(8)}$	—	0.003	—	—
	$c_{HI,2}^{(8)}$	—	0.003	—	—
	$c_{HI}^{(8),(3)}$	—	0.003	—	—
	$c_{He}^{(8)}$	—	0.004	—	—

Table 3. Linear shift in A_ℓ for all dimension-six and dimension-eight Wilson coefficients contributing significantly, for $\Lambda = 1$ TeV. The shifts are shown for SMEFTsim [28], EWPD2dim8 [20], and EWPDatNLO [32] (both at LO and NLO). The comparison is made for the fully flavour symmetric case using the $\{M_W, M_Z, G_\mu\}$ input parameter scheme.

due to the b -quark mass, which is non-zero only for the `SMEFTsim` parametrization, and the limited numerical precision of the tables in Ref. [20], which were used for the `EWPD2dim8` parametrization.

1.6 The EWPD fit in the SMEFT (at NLO)

In this section, the observables introduced in Section 1.1 are analyzed using a parametrization that combines the SM predictions of Section 1.3 with the SMEFT parametrization in Section 1.5 to set limits on dimension-six Wilson coefficients.

This analysis assumes a $U(2)_q \times U(2)_u \times U(2)_d$ symmetry in the quark sector, as there are no observables that allow to distinguish the first two quark generations with high precision. A fully flavour-general fit would result in several blind directions related to differences in light quark couplings. Lepton flavour universality violation is allowed.

Unless noted otherwise, the $\{M_W, M_Z, G_\mu\}$ input parameter scheme is employed. The SM value of $\alpha(Q^2 = M_Z^2)$ is predicted by these input parameters, and potential deviations from this value are constrained by including the semi-experimentally determination of $\Delta\alpha$ as an observable in the fit. Similarly, deviations from the SM prediction of $\sin^2\theta_{\text{eff}}^\ell$ are constrained by measurements of the EWPOs A_e , A_μ , and A_τ as well as the various forward–backward asymmetries. The `EWPDatLO` and `EWPDatNLO` [32] SMEFT parametrizations are employed for this analysis.

While the `ewpd4lhc` tool contains parametrizations up to Λ^{-4} , this analysis focusses on fits using only the Λ^{-2} contributions, which are produced instantaneously when running `ewpd4lhc`. Including Λ^{-4} contributions requires a more complex numerical analysis due to the quadratic dimension-six Wilson coefficient dependence. This is left to a future publication.

In total 30 observables are studied of which six are SM inputs. Figure 4 presents one-dimensional confidence intervals for Wilson coefficients in all five input parameter schemes, derived by fitting one parameter at a time. The first panel displays the limits obtained using the LO SMEFT parametrization. In the second panel, the same 19 Wilson coefficients are analyzed using the NLO SMEFT parametrization. NLO corrections have a relatively small effect on results, typically shifting central values and improving limits by approximately 5%. The scheme dependence is already small at LO — because SM predictions include higher-order corrections — and is reduced further at NLO, particularly in schemes that use M_W as an input. The third panel displays the 24 most stringent constraints on Wilson coefficients that appear only at loop level. Sensitivity exists in particular for operators coupling to the top quark, owing to the larger impact of diagrams involving heavy quark loops. While constraints on loop-level operators, except for c_{Ht} , are generally weaker than those for tree-level operators, they are often more restrictive than limits derived from LHC measurements of top quark production. For instance, in many cases they surpass the constraints from the comprehensive SMEFT analysis of top-quark pair-production with additional leptons performed by CMS [61]. However, the one-at-a-time EWPD constraints rely heavily on a small set of precisely measured observables, leaving numerous blind directions. These blind directions can only be addressed through additional measurements at the LHC.

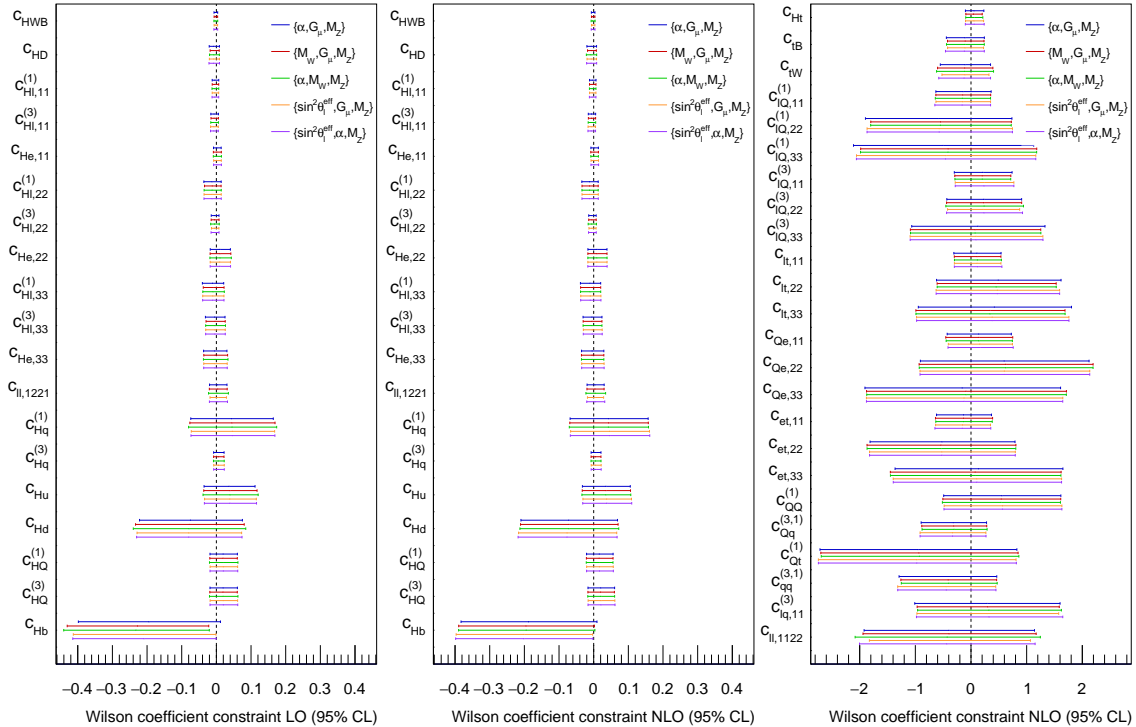


Figure 4. Comparison of one-at-a-time Wilson coefficients constraints in the SMEFT EWPD fit in five different input parameter schemes at $O(\Lambda^{-2})$. A $U(2)_q \times U(2)_u \times U(2)_d$ symmetry between the first two quark generations and $\Lambda = 1\text{ TeV}$ is assumed. For the leftmost panel a LO SMEFT parametrization is employed while the a NLO parametrization is employed for the remaining constraints.

Multi-dimensional fits require extra care as unconstrained directions exist, corresponding to linear combination of Wilson coefficients that do not affect the studied observables. Both constrained and unconstrained directions are identified, with the latter eliminated, through the following procedure. The inverse of the covariance matrix of measurements, V^{-1} (which, for this purpose, includes theoretical and parametric uncertainties as outlined in Section 1.3), is transformed using the linear parametrization matrix $A^{(6)}$ (see Equation 1.10), to obtain the inverse of the covariance matrix in the space of Wilson coefficients:

$$V_{\text{SMEFT}}^{-1} = (A^{(6)})^T V^{-1} A^{(6)}. \quad (1.11)$$

This matrix corresponds to the Fisher information matrix. Its eigenvectors are uncorrelated directions in the Wilson coefficient space and their corresponding eigenvalues, λ , are related to the expected uncertainty σ of a constraint in direction of the eigenvector:

$$\sigma = \frac{1}{\sqrt{\lambda}}. \quad (1.12)$$

At LO there are 16 constrained directions with finite eigenvalues and three unconstrained directions corresponding to zero eigenvalues. Two of the unconstrained directions are Wilson coefficient combinations that cannot be constrained in fermion-fermion

to fermion-fermion scattering alone [47] and one corresponds to a combination of $c_{HQ}^{(1)}$ and $c_{HQ}^{(3)}$ that affects the top but not the bottom quark coupling to weak bosons.

Constrained directions, along with the observables contributing most to each constraint are listed in Table 4. In the eigenvector basis, where correlations are removed and unconstrained directions are eliminated, the best-fit values are determined by solving a system of linear equations. The pulls, defined as the difference of best-fit value and direct measurement, divided by the uncertainty σ , are also shown in Table 4.

The most tightly constrained direction corresponds to the difference between the SM-predicted value of $\alpha(Q^2 = M_Z^2)$ and the experimental value of $\alpha(Q^2 = 0)$ in conjunction with the semi-experimental result on the running to $Q^2 = M_Z^2$. For a BSM physics model that introduces non-zero Wilson coefficients in this direction with $O(1)$ couplings, such that $\sum_i (c_i)^2 = 1$, this corresponds to a sensitivity to a mass scale of about $\frac{1}{\sqrt{0.002}}$ TeV ≈ 20 TeV.

Measurements of W and Z pole observables constrain 15 additional directions at LO, with a precision ranging 0.003 (driven by the hadronic Z pole cross section measurement) to 1 (constrained only by the hadronic W branching fractions). Throughout this paper $\Lambda = 1$ TeV is assumed and results for alternative scales Λ' can be obtained by multiplying with $\left(\frac{\Lambda'}{\text{TeV}}\right)^2$.

The inclusion of additional operators at NLO disrupts some of the relationships that hold between observables. As a result, more independent directions in parameter space exist that can be constrained by EWPD. For example, already in a flavour-universal scenario, the $Z \rightarrow b\bar{b}$ decay rate decouples from the $Z \rightarrow d\bar{d}$ and $Z \rightarrow s\bar{s}$ rate, as it is more strongly influenced by operators modifying quark couplings, due to the more important role of heavy quark loops for this process. Additionally, left-handed Z couplings are related to W couplings (see, e.g., Ref. [62]), enabling at LO the prediction of W branching fractions based on Z boson branching fractions and asymmetries. At NLO, Z decays are influenced by a broader set of four-fermion operators compared to W decays, breaking this relationship.

All constrained direction in the NLO parametrization are summarized in Table 4, too. These directions closely resemble those obtained at LO, with minor changes in numerical coefficients and small corrections from additional Wilson coefficients. Under the studied flavor symmetry, which decouples third-generation quarks already at tree level, one additional direction is constrained at NLO. This direction primarily corresponds to modifications in the c_{tW} and $c_{tQ}^{(3)}$ coefficients, which contribute to NLO diagrams involving top and bottom quarks in loops, some of which are shown in Figure 3. The linear combination primarily consists of Wilson coefficients that contribute only at loop level and does not affect Z decays but can be constrained through the W boson width. However, the sensitivity to this NLO contribution is poor, requiring Wilson coefficients of magnitudes around 20 (for $\Lambda = 1$ TeV) to produce a one-standard-deviation shift in the observed value.

The overall agreement with the SM expectation of no significant deviations from zero is excellent at NLO, corresponding to a p -value of 87%, which is even higher than the LO parametrization p -value of 76%. The analysis does not show substantial evidence of BSM physics. Indeed, there is only one direction in Wilson coefficient space that deviate by more than a standard deviation from zero, a three-standard-deviation excess in a direction

Constrained direction (LO parametrization)	Main contr.	σ	Pull
$0.83c_{HWB} + 0.31c_{HI,22}^{(3)} + 0.31c_{CHD} + 0.25c_{HI,11}^{(3)} - 0.15c_{U,1221} - 0.14c_{He,11}$	$\Delta\alpha$	0.0022	-0.7
$0.68c_{HI,11}^{(1)} + 0.46c_{HI,11}^{(3)} - 0.44c_{He,11} - 0.23c_{Hq}^{(3)} - 0.17c_{HI,22}^{(3)} - 0.12c_{HWB}$	σ_{had}^0	0.0033	-0.6
$0.6c_{Hq}^{(3)} - 0.48c_{HI,22}^{(3)} - 0.36c_{HI,22}^{(1)} + 0.27c_{He,22} + 0.24c_{HWB} - 0.2c_{He,11}$	R_μ, Γ_Z	0.006	0.7
$0.68c_{He,11} + 0.42c_{CHD} - 0.25c_{HI,22}^{(3)} + 0.24c_{HI,11}^{(3)} - 0.23c_{HI,22}^{(1)} + 0.22c_{HI,11}^{(1)}$	$A_e^{\text{SLD}}, A_{\text{FB}}^{0,b}$	0.0092	-0.2
$0.59c_{HI,33}^{(3)} + 0.55c_{HI,33}^{(1)} - 0.31c_{He,33} - 0.31c_{He,11} - 0.19c_{HI,22}^{(3)} - 0.17c_{HI,11}^{(3)}$	R_τ	0.0097	0.0
$0.51c_{HI,22}^{(1)} - 0.42c_{He,22} + 0.36c_{HI,11}^{(1)} + 0.35c_{U,1221} + 0.31c_{Hq}^{(3)} - 0.28c_{HI,11}^{(3)}$	Γ_Z	0.012	-0.5
$0.63c_{HQ}^{(1)} + 0.63c_{HQ}^{(3)} - 0.38c_{Hq}^{(3)} - 0.11c_{HI,11}^{(3)} - 0.1c_{Hb} - 0.09c_{HI,22}^{(3)}$	R_b	0.016	0.4
$0.84c_{He,33} + 0.38c_{CHD} + 0.23c_{HI,33}^{(1)} + 0.18c_{HI,33}^{(3)} - 0.14c_{He,11} - 0.12c_{HI,11}^{(3)}$	A_τ^{LEP}	0.02	-0.5
$0.68c_{He,22} - 0.37c_{HI,11}^{(3)} + 0.36c_{HI,22}^{(3)} + 0.25c_{CHD} + 0.24c_{HI,11}^{(1)} + 0.21c_{HI,22}^{(1)}$	$A_{\text{FB}}^{0,\mu}, R_W^{\mu/e}$	0.033	0.5
$0.64c_{HI,22}^{(1)} - 0.43c_{HI,11}^{(1)} - 0.39c_{HI,22}^{(3)} + 0.35c_{HI,11}^{(3)} + 0.3c_{He,22} - 0.13c_{HI,33}^{(1)}$	$R_W^{\mu/e}$	0.052	-0.3
$0.69c_{HI,33}^{(3)} - 0.49c_{HI,33}^{(3)} - 0.35c_{U,1221} + 0.22c_{Hq}^{(3)} - 0.15c_{He,22} + 0.13c_{HI,22}^{(1)}$	R_e	0.063	0.2
$0.97c_{Hq}^{(1)} + 0.14c_{Hu} - 0.1c_{Hq}^{(3)} - 0.09c_{Hd} + 0.07c_{Hb} - 0.06c_{CHD}$	R_c	0.099	0.1
$0.85c_{Hu} + 0.35c_{U,1221} - 0.17c_{Hq}^{(1)} + 0.14c_{HI,33}^{(1)} + 0.13c_{Hb} - 0.13c_{Hq}^{(3)}$	$A_{\text{FB}}^{0,c}, A_c$	0.14	0.0
$0.77c_{U,1221} - 0.4c_{Hu} - 0.26c_{HI,33}^{(3)} - 0.21c_{HI,11}^{(1)} + 0.2c_{HI,33}^{(1)} - 0.18c_{HI,22}^{(1)}$	$R_W^{\tau/\mu}$	0.15	-0.5
$0.97c_{Hb} - 0.12c_{Hu} + 0.1c_{CHD}$	$A_b, A_{\text{FB}}^{0,b}$	0.23	-3.0
$0.99c_{Hd} + 0.1c_{Hq}^{(1)}$	B_W^μ, B_W^e	1.2	-0.3
Constrained direction (NLO parametrization)	Main contr.	σ	Pull
$0.83c_{HWB} + 0.32c_{HI,22}^{(3)} + 0.31c_{CHD} + 0.25c_{HI,11}^{(3)} - 0.15c_{U,1221} - 0.12c_{He,11}$	$\Delta\alpha$	0.0021	-0.7
$0.67c_{HI,11}^{(1)} - 0.47c_{He,11} + 0.46c_{HI,11}^{(3)} - 0.25c_{Hq}^{(3)} - 0.14c_{HI,22}^{(3)} - 0.11c_{HWB}$	σ_{had}^0	0.0032	-0.7
$0.6c_{Hq}^{(3)} - 0.48c_{HI,22}^{(3)} - 0.35c_{HI,22}^{(1)} + 0.29c_{He,22} + 0.24c_{HWB} - 0.2c_{He,11}$	R_μ, Γ_Z	0.0057	0.7
$0.69c_{He,11} + 0.42c_{CHD} + 0.29c_{HI,11}^{(3)} - 0.25c_{HI,22}^{(1)} + 0.23c_{HI,11}^{(1)} - 0.22c_{HI,22}^{(3)}$	$A_e^{\text{SLD}}, A_{\text{FB}}^{0,b}$	0.0088	-0.3
$0.58c_{HI,33}^{(3)} + 0.55c_{HI,33}^{(1)} - 0.35c_{He,33} - 0.24c_{He,11} - 0.2c_{HI,22}^{(3)} - 0.17c_{HI,11}^{(1)}$	R_τ	0.0093	-0.0
$0.47c_{HI,22}^{(1)} - 0.44c_{He,22} + 0.38c_{HI,11}^{(1)} + 0.33c_{U,1221} + 0.3c_{Hq}^{(3)} - 0.24c_{HI,11}^{(3)}$	Γ_Z	0.012	-0.6
$0.64c_{HQ}^{(1)} + 0.62c_{HQ}^{(3)} - 0.37c_{Hq}^{(3)} - 0.11c_{HI,11}^{(3)} - 0.11c_{Hb} - 0.09c_{HI,22}^{(3)}$	R_b	0.016	0.4
$0.82c_{He,33} + 0.39c_{CHD} + 0.26c_{HI,33}^{(1)} + 0.22c_{HI,33}^{(3)} - 0.13c_{He,11} - 0.12c_{HI,11}^{(3)}$	A_τ^{LEP}	0.019	-0.8
$0.54c_{He,22} + 0.45c_{HI,22}^{(3)} - 0.44c_{HI,11}^{(3)} + 0.35c_{HI,11}^{(1)} + 0.24c_{CHD} - 0.18c_{HI,33}^{(3)}$	$R_W^{\mu/e}, A_{\text{FB}}^{0,\mu}$	0.037	0.5
$0.68c_{HI,22}^{(1)} - 0.35c_{HI,11}^{(1)} + 0.34c_{He,22} - 0.29c_{HI,22}^{(3)} + 0.29c_{HI,11}^{(3)} + 0.18c_{HI,33}^{(1)}$	$R_W^{\mu/e}$	0.055	-0.2
$0.67c_{HI,33}^{(1)} - 0.45c_{HI,33}^{(3)} - 0.35c_{He,22} - 0.33c_{U,1221} + 0.2c_{Hq}^{(3)} - 0.17c_{HI,22}^{(1)}$	R_e	0.063	0.2
$0.99c_{Hq}^{(1)} - 0.09c_{Hd} - 0.09c_{Hq}^{(3)} - 0.04c_{CHD} + 0.04c_{Hb} + 0.03c_{HI,11}^{(3)}$	R_c	0.098	0.0
$0.81c_{U,1221} + 0.28c_{Hu} - 0.24c_{HI,33}^{(3)} + 0.24c_{HI,33}^{(1)} + 0.2c_{HI,11}^{(3)} - 0.19c_{HI,11}^{(1)}$	$R_W^{\tau/\mu}$	0.15	-0.4
$0.91c_{Hu} - 0.26c_{U,1221} - 0.14c_{CHD} - 0.12c_{Hq}^{(3)} + 0.12c_{HI,33}^{(3)} + 0.1c_{HI,11}^{(1)}$	$A_c, A_{\text{FB}}^{0,c}$	0.16	0.4
$0.98c_{Hb}$	A_b	0.27	-2.7
$0.97c_{Hd} + 0.12c_{HQ}^{(3,1)} + 0.11c_{Hq}^{(1)}$	B_W^μ, B_W^e	1.1	-0.3
$0.72c_{tW} + 0.40c_{tQ,22}^{(3)} + 0.38c_{tQ,33}^{(3)} + 0.31c_{tQ,11}^{(3)} - 0.12c_W + 0.12c_{HQ}^{(1)}$	Γ_W	17	0.1

Table 4. Constrained directions in the SMEFT EWPD fit, assuming a $U(2)_q \times U(2)_u \times U(2)_d$ symmetry between the first two quark generations, for $\Lambda = 1$ TeV and at $O(\Lambda^{-2})$, using a LO (top) and NLO SMEFT parametrization (bottom). Linear combinations are normalized and only the five Wilson coefficients with the largest absolute value are shown, provided their absolute value is larger than 0.1. For each direction, the observables that contribute most to an uncorrelated χ^2 for a shift in the eigenvector direction are indicated as “Main contr.,” with a cut-off of at a 20% fractional contribution. The uncertainty σ corresponds to 68% confidence level intervals. The pull is defined as the best-fit value of the Wilson coefficient direction, divided by the uncertainty σ .

predominantly affecting the coupling of the Z boson to right-handed bottom quarks. This deviation is driven by the larger-than-expected values of $A_{\text{FB}}^{0,b}$ and A_b measured at LEP and SLD, respectively. A value of $\frac{c_{Hb}}{\Lambda^2} \approx \frac{1}{\text{TeV}^2}$ would be necessary to match the measurement, which would imply BSM physics that is either strongly coupled or at a relatively low mass scale.

Across all five input parameter schemes, the number of constrained directions remains the same, with constraints and the composition of Wilson coefficients differing only slightly. This consistency validates the NLO parametrizations in alternative schemes as well as the uncertainty model, which is also crucial for scheme-independent results. Despite the near scheme-independence of the likelihood, using a consistent input parameter scheme remains critical when combining results with additional data. Scheme differences could otherwise misalign blind directions, introducing spurious constraints on certain combinations of Wilson coefficients.

To obtain the best-fit values and uncertainties for all observables, error propagation is employed. Sensitive directions that are linear combinations of both the SM input parameters and the Wilson coefficients are fit to the data. Post-fit values for all observables are derived by propagating uncertainties from these combinations. An exception is made for the weakest constrained direction, which only exists at NLO. As it requires unlikely large Wilson coefficient values (or small scales Λ) to affect the data, it is fixed to zero. The results are summarized in Table 5. In most cases, the fit values closely align with direct measurements due to the large number of additional parameters, the Wilson coefficients, that independently modify observables. There are two main exceptions to this. The first exception are A_f and $A_{\text{FB}}^{0,f}$, as well as W boson (ratio of) branching fractions measurements. These are straightforwardly related through Equation 1.3 and Equation 1.4, respectively. The second exception are the total widths of the Z boson and W boson, whose relationship is more complex and will be discussed in the next section.

2 Impact of recent LHC measurements on the EWPD likelihood

In 2024, the ATLAS and CMS collaborations have published three measurements that have provided important updates on weak boson properties. A measurement of the W mass and width [5], the lepton universality of W branching fractions [6], and the effective leptonic weak mixing angle [7].² This section examines how these measurements influence the EWPD likelihood in the SMEFT.

2.1 ATLAS measurement of W boson mass and width

The simultaneous measurement of the W boson mass and width by ATLAS has an important impact on the EWPD likelihood. In Figure 5, the ATLAS measurement is compared with predictions from the SM and SMEFT fits, using the framework described in Section 1.

²While finalizing this paper, a precise measurement of the W mass [43] was presented by the CMS collaboration. It is not considered here as it is a preliminary result and because it assumes, in its current iteration, the SM W width.

Observable	Direct	Fit	Pull	Indirect
M_H [GeV]	125.10 ± 0.11	125.10 ± 0.11	-0.0	–
m_t [GeV]	172.57 ± 0.58	172.57 ± 0.58	0.0	–
α_s	0.11840 ± 0.00080	0.11840 ± 0.00080	0.0	–
M_Z [GeV]	91.1876 ± 0.0021	91.1874 ± 0.0021	-0.1	–
G_μ [10^{-5}GeV^{-2}]	$1.16637880 \pm 0.00000060$	$1.16637880 \pm 0.00000060$	-0.0	–
$\Delta\alpha$	0.059030 ± 0.000090	0.059030 ± 0.000090	-0.0	–
M_W [GeV]	80.369 ± 0.013	80.369 ± 0.013	0.0	–
Γ_Z [GeV]	2.4955 ± 0.0023	2.4955 ± 0.0023	0.0	2.505 ± 0.072
R_e	20.804 ± 0.050	20.786 ± 0.046	-0.3	20.71 ± 0.52
R_μ	20.784 ± 0.034	20.784 ± 0.033	0.0	–
R_τ	20.764 ± 0.045	20.764 ± 0.045	-0.0	–
σ_{had}^0 [pb]	41481 ± 32	41480 ± 32	-0.0	41300 ± 1000
A_e^{SLD}	0.1516 ± 0.0021	0.1494 ± 0.0017	-1.0	0.1459 ± 0.0027
A_e^{LEP}	0.1498 ± 0.0049	0.1494 ± 0.0017	-0.1	0.1494 ± 0.0018
A_μ^{SLD}	0.142 ± 0.015	0.147 ± 0.010	0.3	0.150 ± 0.013
A_τ^{SLD}	0.136 ± 0.015	0.145 ± 0.004	0.6	0.145 ± 0.004
A_τ^{LEP}	0.1439 ± 0.0043	0.1448 ± 0.0040	0.2	0.1510 ± 0.011
$A_{\text{FB}}^{0,e}$	0.0145 ± 0.0025	0.0167 ± 0.0003	0.9	0.0167 ± 0.0003
$A_{\text{FB}}^{0,\mu}$	0.0169 ± 0.0013	0.0164 ± 0.0010	-0.4	0.0160 ± 0.0015
$A_{\text{FB}}^{0,\tau}$	0.0188 ± 0.0017	0.0162 ± 0.0004	-1.5	0.0161 ± 0.0004
R_c	0.1721 ± 0.0030	0.1720 ± 0.0030	-0.0	–
R_b	0.21629 ± 0.00066	0.21630 ± 0.00066	0.0	–
$A_{\text{FB}}^{0,c}$	0.0707 ± 0.0035	0.0734 ± 0.0022	0.8	0.0746 ± 0.0028
A_b	0.923 ± 0.020	0.897 ± 0.015	-1.3	0.871 ± 0.021
A_c	0.670 ± 0.027	0.655 ± 0.022	-0.6	0.634 ± 0.036
$A_{\text{FB}}^{0,b}$	0.0992 ± 0.0016	0.1009 ± 0.0014	1.1	0.1044 ± 0.0024
Γ_W [GeV]	2.085 ± 0.042	2.080 ± 0.017	-0.1	2.079 ± 0.018
B_W^e	0.1071 ± 0.0016	0.1084 ± 0.0010	0.8	0.1085 ± 0.0012
B_W^μ	0.1063 ± 0.0015	0.1087 ± 0.0009	1.6	0.1098 ± 0.0012
B_W^τ	0.1138 ± 0.0021	0.1088 ± 0.0011	-2.4	0.1063 ± 0.0014
$R_W^{\mu/e}$	1.0034 ± 0.0063	1.0031 ± 0.0058	-0.1	1.001 ± 0.015
$R_W^{\tau/e}$	0.994 ± 0.021	1.004 ± 0.010	0.5	1.007 ± 0.011
$R_W^{\tau/\mu}$	0.990 ± 0.011	1.001 ± 0.009	1.0	1.025 ± 0.016

Table 5. Inputs to the EWPD SMEFT fit, alongside the fit results obtained using a NLO SMEFT parametrization. Pull values are calculated as the difference of fit result and direct measurement, divided by the uncertainty of the direct measurement. The column labeled “indirect” contains the result of a fit that does not include the direct measurement corresponding to each respective row. A dash indicates that the indirect prediction is impossible or possible only with very poor precision.

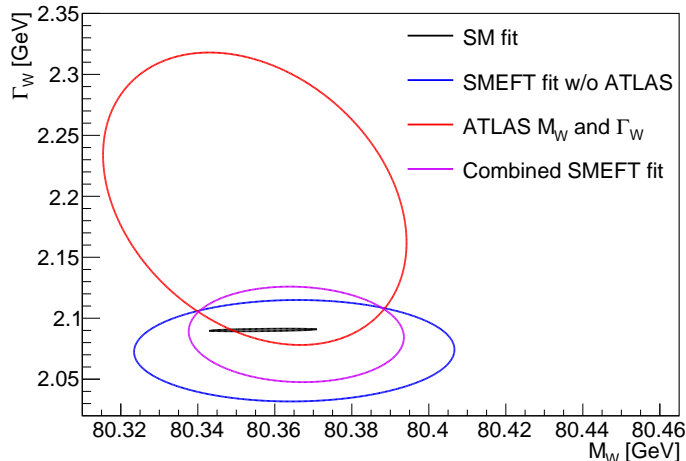


Figure 5. The SM fit result for M_W and Γ_W compared to the direct ATLAS measurement and SMEFT fit results at $O(\Lambda^{-2})$, without assuming flavour universality. The SMEFT fits are performed with and without the ATLAS measurement, to demonstrate its impact. Only variations of Wilson coefficient that have a significant effect for values of $\frac{c_i}{\Lambda^2} \lesssim \frac{1}{\text{TeV}^2}$ are considered. The value of M_W in the SMEFT fit corresponds to the combination of direct measurements, as indirect constraints are weak while both direct and indirect constraints exist for Γ_W .

Without ATLAS data, the M_W used as input to the fit is a combined value from measurements from LEP [63], D0 [64], and LHCb [65], as the PDG average already contains an ATLAS measurement of M_W [66] that is superseded by Ref. [5] while the CDF measurement is excluded due to incompatibility [67]. The combination uses the CT18 set of parton distribution functions (PDFs), in line with the procedure of the LHC-TeV M_W working group [67], resulting in combined value of $M_W^{\text{direct, no ATLAS}} = 80.365 \pm 17 \text{ GeV}$.

In the SM, both M_W and Γ_W can be predicted with higher precision than direct measurements achieve. Consequently, incorporating the ATLAS measurement has small effect on M_W (that is not shown in Figure 5) while its impact is negligible for Γ_W .

However, in the SMEFT framework, M_W cannot be predicted indirectly with high precision. The SM value of M_W is determined, at tree level, by α , M_Z , and G_μ , but in the SMEFT M_W also depends on multiple Wilson coefficients. This dependence arises from field redefinitions necessary in the presence of certain dimension-six operators and from modifications to the muon decay rate used to determine G_μ , which receives contributions from operators affecting W couplings to leptons and an operator introducing a four-fermion interaction [26]. As a result, the SMEFT fit without the ATLAS data yields an M_W value identical to the LEP+D0+LHCb combination of direct measurements.

The ATLAS measurement, being more precise than the combination of other direct measurements (as long as the CDF and CMS results are excluded), substantially enhances the precision of M_W in the SMEFT. In input parameter schemes that exclude M_W , this directly constrains the combination of Wilson coefficient that influences M_W , providing one of the leading constraints on BSM physics. In the schemes including M_W , this improvement results in more precise SM predictions, equally improving SMEFT constraints.

In contrast, Γ_W in the SMEFT can be predicted, at least at LO, with higher precision indirectly than is possible with direct measurements (albeit much lower than the precision of the SM prediction).³ This prediction relies on two central SMEFT assumptions: that the SM gauge symmetries are valid — relating W and Z couplings, allowing for the translation of the more precise Z coupling constraints to W coupling constraints — and that there are no new light states into which SM particles, including the W boson, could decay. Although the ATLAS measurements of Γ_W is nearly as precise as the combination of previous direct measurements, its impact on the global SMEFT fit is modest because the indirect SMEFT prediction for Γ_W has a precision of 18 MeV precision, compared to the 49 MeV precision of the ATLAS measurement.

If NLO corrections to SMEFT parametrizations are taken into account, it is generally no longer possible to predict Γ_W indirectly. However, as discussed in Section 1.6, observable modifications to Γ_W would require extremely large Wilson coefficient values for operators appearing exclusively at loop level, particularly c_{tW} and $c_{tQ}^{(3)}$, which are largely excluded by measurements of $t\bar{t}W$ production. This non-trivial relationship between the W boson width and the $t\bar{t}W$ production cross-section further underscores the importance of combining EWPD and LHC data. For Figure 5, the weakly constrained linear combination involving c_{tW} and $c_{tQ}^{(3)}$ has been fixed to zero, consistent with the approach described in the previous section.

The publication of the correlation of the W boson mass and width measurements is of particular importance for the SMEFT analysis. The SMEFT fit prefers a lower value of Γ_W than ATLAS, which, due to the negative correlation between M_W and Γ_W , leads to a larger M_W value. In fact, the global SMEFT fit result is 6 MeV larger than it would be if zero correlation were assumed for the ATLAS M_W and Γ_W measurements. Furthermore, the uncertainty in M_W in the SMEFT fit is larger than it would be if the SM width were assumed in its extraction, but smaller than the uncertainty that would result from a fit that is agnostic of Γ_W .

Intriguingly, the ATLAS measurement of Γ_W deviates by about two standard deviations from the SM prediction. However, this deviation cannot be attributed to BSM physics compatible with SMEFT assumptions, as the SMEFT fit, even with the ATLAS data included, aligns closely with the SM value of Γ_W .

³It can be shown straightforwardly demonstrated this is sensible, using the known dimension-six Wilson coefficient dependence of only a few observables. Specifically, in the $\{M_W, M_Z, G_\mu\}$ scheme, the relative deviation in the leptonic W branching fraction due to dimension-six Wilson coefficients is a linear combination (with strictly positive coefficients) of the relative deviation from the SM expectation of α , the invisible Z width and the partial width of the Z boson for decays into left-handed leptons (the decay rate into left-handed leptons can be inferred from the partial Z boson widths, in combination with the asymmetry parameters A_ℓ). All three quantities are measured with a precision of 0.5% or better. Consequently, the partial $W \rightarrow \ell\nu$ width can be predicted with even higher precision. By dividing this result by $\mathcal{B}(W \rightarrow \text{leptons})$ yields Γ_W , where the uncertainty of this Γ_W prediction is primarily determined by the 0.8% uncertainty in the measurement of the leptonic branching fraction.

2.2 ATLAS measurement of lepton flavour universality in W decays

Another precise measurement of W boson properties recently published by ATLAS is the precise study of lepton flavour universality in W decays [6]. The ratio of W branching fractions $R_W^{\mu/e}$ is determined with an exceptional precision of 0.45%. This ratio, which compares the W boson decays into muons and neutrinos against electrons and neutrinos, is sensitive to anomalous couplings of the W boson to leptons. In the framework of the SMEFT it constrains exactly two Warsaw basis Wilson coefficients (at LO — the small NLO contributions are discussed at the end of this section):

$$R_W^{\mu/e} = \frac{\mathcal{B}(W \rightarrow \mu\nu)}{\mathcal{B}(W \rightarrow e\nu)} \approx 1 + 2\delta g^{W\mu} - 2\delta g^{We} = 1 + \frac{2v^2}{\Lambda^2} \left(c_{H\ell,22}^{(3)} - c_{H\ell,11}^{(3)} \right), \quad (2.1)$$

where, $g^{W\ell}$ is the dimensionless coupling of the W to a charged lepton ℓ and its corresponding neutrino, and $\delta g^{W\ell}$ denotes its deviation from the SM expectation. The approximation $\Gamma(W \rightarrow \ell\nu) = \Gamma_{\text{SM}}(W \rightarrow \ell\nu)(1 + \frac{\delta g_W}{g_W})^2 \approx \Gamma_{\text{SM}}(W \rightarrow \ell\nu)(1 + 2\frac{\delta g^{W\ell}}{g^{W\ell}})$ is used. In contrast to the total width, partial widths for individual lepton flavours cannot be inferred from Z boson measurements. This would require flavour-specific measurements of Z boson decays to neutrinos, when only the inclusive invisible width can be observed.

To mitigate uncertainties in lepton identification, ATLAS does not directly measure $R_W^{\mu/e}$ but instead fits the parameter

$$R_{WZ}^{\mu/e} = R_{WZ}^{\mu/e} / \sqrt{R_Z^{\mu/e}}, \quad (2.2)$$

where $R_Z^{\mu/e}$ represents the ratio of Z boson branching fractions into muon and electron pairs. This ratio is combined with the $R_Z^{\mu/e}$ result from LEP+SLD, which has its own SMEFT parameter dependence:

$$\begin{aligned} R_Z^{\mu/e} &= \frac{\mathcal{B}(Z \rightarrow \mu^+\mu^-)}{\mathcal{B}(Z \rightarrow e^+e^-)} \approx 1 - 4\delta g_A^{Z\mu} + 4\delta g_A^{Ze} \\ &= 1 + \frac{2v^2}{\Lambda^2} \left(c_{H\ell,22}^{(3)} - c_{H\ell,11}^{(3)} + c_{H\ell,22}^{(1)} - c_{H\ell,11}^{(1)} - c_{He,22} + c_{He,11} \right), \end{aligned} \quad (2.3)$$

where the dependence $\Gamma(Z \rightarrow \ell\ell) \propto (g_V^{Z\ell})^2 + (g_A^{Z\ell})^2$ of the Z boson partial width on the the vector coupling $g_V^{Z\ell} \approx 0$ and axial vector couplings $g_A^{Z\ell} \approx -0.5$ to leptons is used.

The precise ATLAS measurement constrains the following linear combinations of couplings and Wilson coefficients:

$$\begin{aligned} R_{WZ}^{\mu/e} &= \frac{\mathcal{B}(W \rightarrow \mu\nu)}{\mathcal{B}(W \rightarrow e\nu)} / \sqrt{\frac{\mathcal{B}(Z \rightarrow \mu\mu)}{\mathcal{B}(Z \rightarrow ee)}} \approx 1 + 2\delta g^{W\mu} - 2\delta g^{We} + 2\delta g_A^{Z\mu} - 2\delta g_A^{Ze} \\ &= 1 + \frac{v^2}{\Lambda^2} \left(c_{H\ell,22}^{(3)} - c_{H\ell,11}^{(3)} - c_{H\ell,22}^{(1)} + c_{H\ell,11}^{(1)} + c_{He,22} - c_{He,11} \right). \end{aligned} \quad (2.4)$$

The Wilson-coefficient dependence is similar to that of of $R_Z^{\mu/e}$, but it is a factor of two weaker, with the signs of $c_{H\ell,22}^{(1)}$ and $c_{H\ell,11}^{(1)}$ flipped. Hence the observable constrains an

independent direction in Wilson coefficient space while leaving a third direction in the space of LFU violating Wilson coefficients unconstrained.

Without the inclusion of the ATLAS measurement, the global SMEFT fit yields a value of $R_{WZ}^{\mu/e} = 1.0027 \pm 0.0059$, which is slightly less precise than the constraint of $R_W^{\mu/e}$ (as shown in Table 5). This indicates that a $R_{WZ}^{\mu/e}$ measurement actually has a more significant impact on the SMEFT fit than a measurement of $R_W^{\mu/e}$ with the same precision. When the ATLAS $R_{WZ}^{\mu/e}$ measurement is included, the global fit result — and consequently the constraint on the corresponding direction in Wilson coefficient space — is improved to $R_{WZ}^{\mu/e} = 1.0003 \pm 0.0034$.

For completeness, the LO Wilson coefficient dependence of e - μ universality violating anomalous W and Z couplings is given below, based on Ref. [29] and using $g_{V/A}^{Z\ell} = g_R^{Z\ell} \pm g_L^{Z\ell}$:

$$\delta g^{W\mu} - \delta g^{We} = \frac{v^2}{\Lambda^2} \left(c_{H\ell,22}^{(3)} - c_{H\ell,11}^{(3)} \right), \quad (2.5)$$

$$\delta g_V^{Z\mu} - \delta g_V^{Ze} = \frac{v^2}{2\Lambda^2} \left(-c_{H\ell,22}^{(3)} + c_{H\ell,11}^{(3)} - c_{H\ell,22}^{(1)} + c_{H\ell,11}^{(1)} - c_{He,22} + c_{He,11} \right), \quad (2.6)$$

$$\delta g_A^{Z\mu} - \delta g_A^{Ze} = \frac{v^2}{2\Lambda^2} \left(c_{H\ell,22}^{(3)} - c_{H\ell,11}^{(3)} + c_{H\ell,22}^{(1)} - c_{H\ell,11}^{(1)} - c_{He,22} + c_{He,11} \right). \quad (2.7)$$

2.3 CMS measurement of the effective leptonic weak mixing angle

The CMS collaboration recently presented a new measurement of the effective leptonic weak mixing angle, $\sin^2 \theta_{\text{eff}}^\ell$ [7]. Unlike the measurements of W mass and width, which focus on fairly model-independent characteristics of the reconstructed distributions (see also the discussion in Ref. [68]), and the W branching fraction measurements, which constrains inclusive rates, the $\sin^2 \theta_{\text{eff}}^\ell$ measurement does not lend itself to straightforward interpretation within the SMEFT framework. This is because the measurement relies on a mass-dependent analysis of the forward–backward asymmetry in Drell–Yan events, which in the SMEFT context involves a non-trivial dependence not only on lepton but also on quark couplings and four-fermion operators. Moreover, the measurements in the electron and muon channels have different Wilson coefficient dependencies, preventing their combination in the SMEFT.

However, the CMS measurement can be reinterpreted as one of the most precise test of lepton-flavour universality. It is primarily sensitive to vector couplings of the Z boson, thus constraining the third Wilson combinations combination left unconstrained by the $R_Z^{\mu/e}$ and $R_{WZ}^{\mu/e}$ measurements.

For the LFU interpretation, the ratio of $\sin^2 \theta_{\text{eff}}^\ell$ measurements in muon and electron channel is denoted $R_{\sin^2 \theta_{\text{eff}}^\ell}^{\mu/e}$. The exact value implied by the CMS measurement is difficult to determine without a detailed correlation model for the systematic uncertainties. An estimate based on leptons reconstructed in the central part of the detector (see Table 4 of Ref. [7]), which offers similar coverage for electrons and muons, yields a value of $R_{\sin^2 \theta_{\text{eff}}^\ell}^{\mu/e} = 0.9987 \pm 0.0012$ (stat.) ± 0.0010 (syst.). This estimate assumes that theoretical and PDF uncertainties cancel due to the similarity in phase space between electron and muon channel measurements. While some theory uncertainties might affect only one lepton species and PDF uncertainties may not be fully correlated due to differences in lepton acceptance and

identification efficiency, these effects are expected to be small. For sensitivity estimation, this approach is considered conservative, as a more rigorous analysis, including electrons reconstructed in the forward part of the detector, could further improve the precision. However, a critical caveat involves the central value of this estimate. During the CMS determination of the $\sin^2 \theta_{\text{eff}}^\ell$ results in electron and muon channel, nuisance parameters, such as those related to the PDFs, will likely be pulled to different central values, which can differently affect $\sin^2 \theta_{\text{eff}}^\ell$ in each channel, whereas consistent parameters should be used in the derivation of $R_{\sin^2 \theta_{\text{eff}}^\ell}^{\mu/e}$.

The uncertainty in the extraction of $R_{\sin^2 \theta_{\text{eff}}^\ell}^{\mu/e}$ is dominated by statistical uncertainties and can be straightforwardly improved with future measurements utilizing larger datasets. In fact, a large part of the systematic uncertainty in the CMS measurement also arises from statistical limitations due to the finite size of Monte Carlo simulated samples. In a dedicated LFU analysis, these uncertainties could be mitigated by using identical parton level events (i.e. events before simulating final state photon radiation or detector and reconstruction effects that differentiate electrons and muons) for analyzing electron and muon channels, or by reweighting simulated distributions to match channels at parton level, resulting in correlated Monte Carlo statistical uncertainties that cancel in the ratio $R_{\sin^2 \theta_{\text{eff}}^\ell}^{\mu/e}$.

Using the relationship

$$\frac{g_V^{Zf}}{g_A^{Zf}} = 1 - 4|Q_f| \sin^2 \theta_{\text{eff}}^f \quad (2.8)$$

(see e.g. Ref. [4]) as well as $\frac{g_V^{Z\ell}}{g_A^{Z\ell}} \ll 1$, and $g_A^{Z\ell} \approx -0.5$ one finds:

$$R_{\sin^2 \theta_{\text{eff}}^\ell}^{\mu/e} = \frac{\sin^2 \theta_{\text{eff}}^\mu}{\sin^2 \theta_{\text{eff}}^e} \approx \frac{1 - \frac{g_V^{Z\mu}}{g_A^{Z\mu}}}{1 - \frac{g_V^{Ze}}{g_A^{Ze}}} \approx 1 - \frac{g_V^{Z\mu}}{g_A^{Z\mu}} + \frac{g_V^{Ze}}{g_A^{Ze}} \approx 1 + 2 \left(g_V^{Z\mu} - g_V^{Ze} \right) \quad (2.9)$$

$$= 1 + \frac{v^2}{\Lambda^2} \left(-c_{H\ell,22}^{(3)} + c_{H\ell,11}^{(3)} - c_{H\ell,22}^{(1)} + c_{H\ell,11}^{(1)} - c_{He,22} + c_{He,11} \right). \quad (2.10)$$

The measurement of the observable evidently constrains a direction in Wilson coefficients space that is linearly independent of the constraints from $R_Z^{\mu/e}$ and $R_{WZ}^{\mu/e}$.

With the experimental result of $R_{\sin^2 \theta_{\text{eff}}^\ell}^{\mu/e} = 0.9987 \pm 0.0016$ it is thus possible to determine the difference in the vector couplings of muons and electrons with high precision. A more accurate expansion of Equation 2.9 that takes into account a non-zero SM value of $g_V^{Z\mu}$ yields

$$g_V^{Z\mu} - g_V^{Ze} = \left(g_A^{Z\ell, \text{SM}} - g_V^{Z\ell, \text{SM}} \right) \left(1 - R_{\sin^2 \theta_{\text{eff}}^\ell}^{\mu/e} \right) = 0.46 \left(R_{\sin^2 \theta_{\text{eff}}^\ell}^{\mu/e} - 1 \right) \quad (2.11)$$

from which one obtains

$$g_V^{Z\mu} - g_V^{Ze} = (-6 \pm 7) \times 10^{-4}. \quad (2.12)$$

This over three times more precise than the current difference in PDG values for $g_V^{Z\mu}$ and g_V^{Ze} , which is $(15 \pm 23) \times 10^{-4}$. Combining the electron vector coupling measurement from

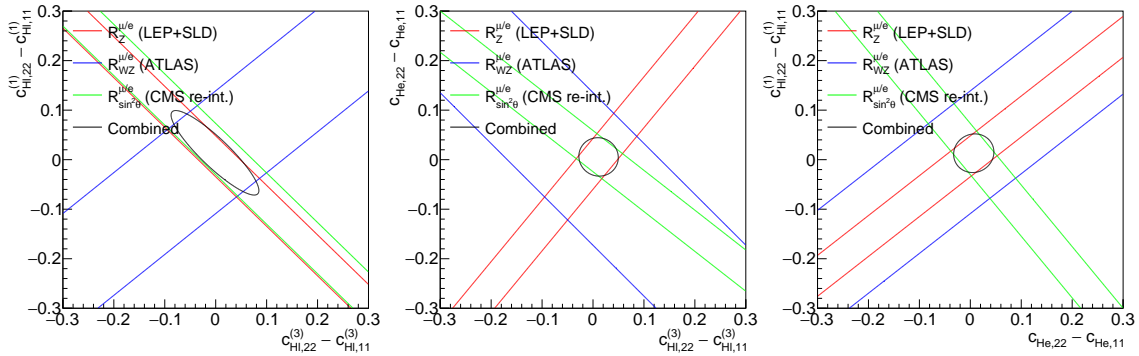


Figure 6. Constraints on the three Wilson coefficient combination introducing leading-order e - μ lepton-flavour universality violating effects in weak boson couplings, at 95% confidence level, for $\Lambda = 1$ TeV. The Wilson coefficient combination not shown in each of the plots is fixed to zero. The impact of the LEP+SLD measurement of $R_Z^{\mu/e}$ [4], the ATLAS measurement of $R_{WZ}^{\mu/e}$ [6], and the reinterpretation of the CMS weak mixing angle measurement [7] as a measurement of $R_{\sin^2\theta_{\text{eff}}^{\mu/e}}$ is compared. For the individual ratio measurements, only one degree of freedom is constrained. Hence, the corresponding confidence intervals are based on a one-dimensional χ^2 distribution. Confidence intervals for the combination correspond to a two-dimensional χ^2 distribution.

LEP+SLD with the above coupling-difference constraint also yields an improved determination of the muon coupling to the Z boson:

$$g_V^{Z\mu} = (-382 \pm 4 - 6 \pm 7) \times 10^{-4} = (-388 \pm 8) \times 10^{-4}. \quad (2.13)$$

This result improves on the precision of the PDG value by a factor of three. As it depends only weakly on theoretical uncertainties and is statistically limited it can be further improved with a larger dataset or by an ATLAS measurement. The main caveats in this derivation are the assumptions that four-fermion operators or anomalous quark couplings have no significant impact, which is likely a reasonable approximation, and that PDF pulls match between the electron and muon channels in Ref. [7], which cannot be validated externally and requires a dedicated fit of $R_{\sin^2\theta_{\text{eff}}^{\mu/e}}$ by the CMS collaboration.

2.4 Comparison of lepton flavour universality tests

In `ewpd41hc` the exact NLO Wilson coefficient dependence of $R_{WZ}^{\mu/e}$, $R_Z^{\mu/e}$, and $R_{\sin^2\theta_{\text{eff}}^{\mu/e}}$ on the three types of Wilson coefficients is implemented, which is used to derive confidence levels for Wilson coefficients in Figure 6. It is clear from the three plots that each of the three observables is almost perfectly suited to constrain a direction in parameter space that is unconstrained by the other two observables.

The constraints based on $R_Z^{\mu/e}$ and $R_{\sin^2\theta_{\text{eff}}^{\mu/e}}$, of which only the latter can be improved in the near future, are more precise than those based on $R_{WZ}^{\mu/e}$. A dedicated measurement of $R_{\sin^2\theta_{\text{eff}}^{\mu/e}}$ by either ATLAS or CMS thus clearly has the potential to become the most precise test of lepton flavour universality.

At NLO, additional Wilson coefficients contribute, although their impact is at least a factor of 40 smaller compared to the Wilson coefficients contributing at tree level. The

most interesting and numerically largest contributions arise due to four-fermion operators coupling top quark and leptons, $c_{lQ}^{(1)}$, $c_{lt}^{(1)}$, $c_{lQ}^{(3)}$, c_{et} , and c_{Qe} . While $c_{lQ}^{(1)}$ and $c_{lt}^{(1)}$ as well as c_{et} and c_{Qe} cannot be distinguished by the three observables, the remaining three directions are constrained by the three types of measurements, similar to the LO Wilson coefficients.

3 Interpretation of the ATLAS Drell–Yan triple-differential cross-section measurement and impact on the global EWPD fit

In the previous section the measurement of $R_{\sin^2 \theta_{\text{eff}}^{\ell}}^{\mu/e}$ was identified as the potentially most precise test of the lepton flavour universality of weak boson couplings. However, certain approximations were necessary to extract couplings values from the CMS measurement of $\sin^2 \theta_{\text{eff}}^{\ell}$. For instance, it was assumed that some systematic uncertainties as well as quark-coupling-modifying operators affect electron and muon channels identically and thus do not interfere in the interpretation of $R_{\sin^2 \theta_{\text{eff}}^{\ell}}^{\mu/e}$. Moreover, the influence of four-fermion operators directly coupling quarks to leptons was ignored. In this section, a more accurate analysis of the forward–backward asymmetry will be performed that accounts for all relevant SMEFT operators and employs a detailed correlation model for systematic uncertainties. This approach will demonstrate that such an analysis can not only test flavour universality but also constrain anomalous quark couplings.

The ATLAS triple-differential cross-section measurement of Drell–Yan production [8], based on LHC Run 1 data at 8 TeV, will be analyzed for this purpose. This model-independent and granular cross-section measurement, published with a detailed breakdown of systematic uncertainties in each analysis channel, allows for an accurate interpretation in the SMEFT.

A SMEFT analysis of Z production at the LHC was previously performed in Ref. [62], with a focus on quark couplings only and a greatly simplified uncertainty model.

3.1 Analysis setup

In Drell–Yan production of a lepton pair in hadron collision, a forward–backward asymmetry exists for the direction of the outgoing leptons. Depending on the invariant mass of the lepton pair, the outgoing negatively charged lepton is emitted either more or less frequently in the direction of the incoming quark (as opposed to anti-quark). This asymmetry is caused by the parity-violating couplings of the Z boson. Near the Z pole, the asymmetric contribution to the Drell–Yan cross-section is, at leading order, proportional to the product of the Z boson axial vector couplings and vector couplings to the colliding quarks and leptons, $g_V^{Zq} g_A^{Zq} g_V^{Z\ell} g_A^{Z\ell}$ (see for example Equation 3 of Ref. [69]). The pole asymmetry is particularly sensitive to variations in the vector coupling of leptons, $g_V^{Z\ell}$, as the coupling is close to zero in the SM. Away from the Z pole, the asymmetry is primarily caused by the interference between Z boson and γ^* mediated amplitudes, which is proportional to the Z boson axial vector couplings to the two fermion types and their photon couplings. The sensitivity of the forward–backward asymmetry to lepton couplings enables precise measurements of the effective leptonic weak mixing angle, $\sin^2 \theta_{\text{eff}}^{\ell}$, which is related to fermion couplings according to Equation 2.8.

ATLAS measured [8] the Drell–Yan cross-section as a function of three observables: the invariant mass of the lepton pair, $m_{\ell\ell}$, the absolute dilepton rapidity, $|y_{\ell\ell}|$, and the angular variable $\cos\theta^*$. In the dilepton centre-of-mass frame, θ^* is defined as the angle of the outgoing negatively charged lepton to the longitudinal boost direction of the dilepton system. The longitudinal boost direction typically corresponds to the incoming valence quark direction, so $\cos\theta^*$ exhibits the forward–backward asymmetry described above. The asymmetry is more pronounced for large values of $|y_{\ell\ell}|$, where the boost direction is more likely aligned with the valence quark direction.

The ATLAS measurement was performed in three analysis channels: with a pair of muons reconstructed in the central part of the detector, a pair of electrons reconstructed in the central detector, and a pair of electrons with one reconstructed in the central and the other in the forward part of the detector. While the measurement of forward electrons is experimentally challenging, it offers sensitivity to dilepton pairs highly boosted along the beam direction, for which the asymmetry is less likely to be diluted by a misassignment of the quark direction.

Over 1000 data points were reported by ATLAS and are available, together with the impact of various sources of uncertainties, on the HEPData webpage.⁴ To reduce the complexity of the presented interpretation, some data points were merged. Instead of analyzing the full $\cos\theta^*$ dependence of the cross-section, only the forward–backward asymmetry A_{FB} is considered. It is calculated in each $m_{\ell\ell} \times |y_{\ell\ell}|$ bin as the cross-section of $\cos\theta^* > 0$ events minus the cross-section of $\cos\theta^* < 0$ events, divided by the total cross-section in that bin. While the integration over $\cos\theta^*$ bins reduces the statistical power of the analysis, it simplifies the analysis considerably. Rapidity bins are combined such that the resulting data points correspond to a bin width of at least 0.8 in $|y_{\ell\ell}|$, which is sufficient to capture rapidity increase of A_{FB} . The full granularity of the $m_{\ell\ell}$ binning is retained, as SMEFT operators exhibit strong mass dependence. The lowest mass bin, measured only in the central–central lepton channels, is omitted due to its limited sensitivity to $\sin^2\theta_{\text{eff}}^\ell$ or dimension-six operators. This procedure reduces the number of analyzed data points to 51: 15 in the e^+e^- central–forward channel and 18 in the central–central channels.

More than 300 unique sources of systematics affect the measurement, with the dominant ones affecting lepton identification and momentum measurement. The effect of each source on the merged analysis bins is determined and used to create a 51×51 covariance matrix for the subsequent statistical analysis.

A SM prediction of Drell–Yan production is generated at next-to-leading order QCD in the POWHEG BOX framework [70, 71] with the NNPDF3.1NNLO set of parton distribution functions [72]. Higher-order corrections to $\sin^2\theta_{\text{eff}}^\ell$ are taken into account by setting the weak mixing angle to 0.23130, the SM value predicted from the measurements of $\{M_W, M_Z, G_\mu\}$ using the formulas discussed in Section 1.2. The linear dependence on M_W is included as a parametric uncertainty in the analysis, while the smaller variation due to other SM input quantities is neglected.

The dominant uncertainty in the SM prediction originates from PDFs, stemming from

⁴<https://www.hepdata.net/record/77492>

uncertainties in the relative contributions of up-quark and down-quark initial states to Drell–Yan production and their predicted momentum fractions. Due to different SM couplings, up-quark and down-quark final states yield different asymmetries while other quark flavours create no asymmetry as quarks and anti quarks carry, on average, equal momentum. Additionally, the distribution of the momentum fraction carried by up and down (anti) quarks affects the number of events in which the anti quark carries a larger momentum fraction than the valence quark, diluting the observable asymmetry. PDF uncertainties are propagated using the Hessian variations of the PDF set and incorporated into the statistical analysis using nuisance parameters with Gaussian constraints.

The values of A_{FB} extracted from the measurement, as well as the SM prediction and their respective uncertainties, were validated against the measurement and predictions published by ATLAS [8], using a matching PDF and value for $\sin^2 \theta_{\text{eff}}^\ell$. Excellent agreement for the measured value was found, for which however only a combination of electron and muon channel is published. Good agreement was also found for the theoretical predictions, despite the absence of NNLO QCD and NLO EW k-factors, which are applied only for the ATLAS prediction.

The linear impact of dimension-six operators on A_{FB} is calculated at leading order and in the $\{M_W, M_Z, G_\mu\}$ input parameter scheme using `MadGraph5_aMC@NLO` with the `SMEFTsim 3.0` model. As in the EWPD fit presented in the first part of the paper, a $U(2)_q \times U(2)_u \times U(2)_d$ asymmetry is assumed in the generation of SMEFT effects. Variations of up-quark and down-quark couplings are thus always accompanied by the same variation of charm-quark and strange-quark couplings. As the latter are symmetric in $\cos \theta^*$, A_{FB} is diluted and the sensitivity to light quark couplings is slightly weaker than in a fully flavour general approach.

Figure 7 shows the difference between the measured A_{FB} and the SM prediction, denoted as ΔA_{FB} . The figure also displays the deviations from the nominal values introduced by systematic uncertainties and dimension-six operators. The data is in good agreement with the SM prediction. Systematic uncertainties are large, in particular in the central–forward e^+e^- channel due to experimental challenges in forward-electron identification. In the $\mu^+\mu^-$ channel, uncertainties are large for more forward events, mainly due to the sagitta bias, which results from potential detector misalignment and introduces a charge-dependent muon momentum uncertainty. PDF uncertainties are minimal in the bin below the Z pole and increase on either side. Variations in M_W affect the SM prediction of the weak mixing angle, leading to shifts in the predicted asymmetry.

For a fixed value of M_W , the Wilson coefficients c_{HWB} and c_{HD} modify the couplings of all fermions to both the Z boson and the photon, thereby influencing A_{FB} . The coefficient c_{He} affects only couplings of the Z boson to right-handed leptons while $c_{Hl}^{(1)}$ and $c_{Hl}^{(3)}$ affect the coupling of the Z boson to charged left-handed leptons. The effect of $c_{Hl}^{(1)}$ and $c_{Hl}^{(3)}$ on Z boson couplings to charged leptons is identical but only the latter affects α , leading to a small difference in their influence on A_{FB} . On the Z pole, the sensitivity is maximal for a simultaneous increase of left-handed and right-handed lepton couplings, which corresponds to a modification of the vector coupling, while the sensitivity to changes in opposite direc-

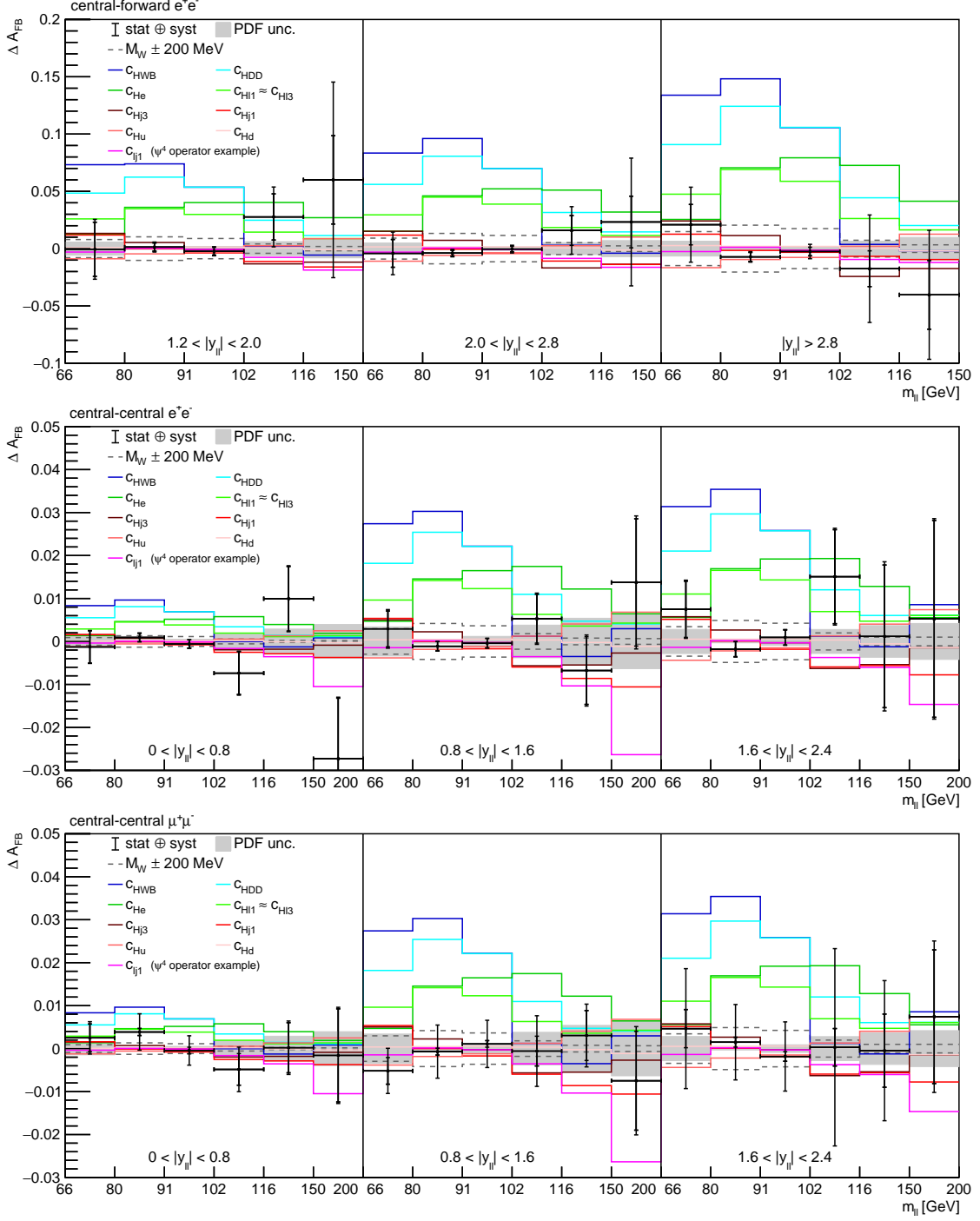


Figure 7. Difference between the measured [8] forward–backward asymmetry A_{FB} in Drell–Yan production in 8 TeV proton–proton collisions and the SM prediction. The linearized shifts in A_{FB} due to systematic uncertainties and dimension-six Wilson coefficients, for $\frac{c_i}{\Lambda^2} = \frac{1}{\text{TeV}^2}$, are also shown. The panels display, from top to bottom, the central–forward e^+e^- , central–central e^+e^- , and central–central $\mu^+\mu^-$ channels. The inner error bars of data points represent the statistical uncertainty while the outer error bars represent the total uncertainty of the measurement. The impact of the Wilson coefficient $c_{HI}^{(1)}$ closely matches the impact of $c_{HI}^{(3)}$. Similarly, the effect of the various four-fermion operators is comparable, with only $c_{lq}^{(1)}$ shown as an representative example.

$\sin^2 \theta_{\text{eff}}^\ell [10^{-5}]$	ATLAS A_4	Interpretation of ATLAS Z3D
Central–forward e^+e^-	$23166 \pm 29 \pm 23 \pm 22$	$23189 \pm 36 \pm 29 \pm 22$
Central–central e^+e^-	$23148 \pm 48 \pm 31 \pm 37$	$23169 \pm 58 \pm 26 \pm 38$
Central–central $\mu^+\mu^+$	$23123 \pm 40 \pm 27 \pm 35$	$23099 \pm 41 \pm 40 \pm 35$
Combined	$23140 \pm 21 \pm 16 \pm 24$	$23167 \pm 24 \pm 20 \pm 24$

Table 6. Comparison of the value of $\sin^2 \theta_{\text{eff}}^\ell$ (in units of 10^{-5}) extracted by ATLAS in Ref. [73] in an analysis based on the measurement of the angular coefficient A_4 and the extraction based on the Drell–Yan triple-differential cross-section measurement (Z3D) [8] performed in this paper. Uncertainties correspond, in order, to statistical, systematic, and PDF uncertainties.

tions, which corresponds to a modification of the lepton axial vector coupling, is relatively small. The coefficients c_{Hu} and c_{Hd} modify the couplings of right-handed up and down quarks to the Z boson, respectively, while $c_{Hq}^{(1)}$ and $c_{Hq}^{(3)}$ affect left-handed quark couplings. The greater sensitivity to modifications in lepton couplings compared to quark couplings is evident. Seven four-fermion operators ($c_{lq}^{(1)}$, $c_{lq}^{(3)}$, c_{lu} , c_{ld} , c_{eu} , c_{ed} , and c_{qe}) couple up and down quarks to leptons of various chirality. For clarity, only one of these operators is shown as an example in the figure. The impact of the four-fermion operators on A_{FB} increases strongly with the invariant mass and is suppressed near the Z pole. All operators except c_{HWB} and c_{HD} carry fermion indices that are not explicitly shown, with operators with subscript 11 (22) affecting electron (muon) channel only.

3.2 Extraction of the effective leptonic weak mixing angle

Before discussing the SMEFT interpretation of the data, this section presents an extraction of the effective leptonic weak mixing angle using the setup described above. The ATLAS collaboration has previously measured $\sin^2 \theta_{\text{eff}}^\ell$ using the 8 TeV dataset [73], which serves as a benchmark of the methodology of this analysis. However, the ATLAS analysis used a different approach, where multiple angular coefficients of the Drell–Yan cross-section were simultaneously extracted in a fit. The value of the angular coefficient A_4 , which quantifies the $\cos \theta^*$ dependence of the cross-section, was used to determine $\sin^2 \theta_{\text{eff}}^\ell$. Differences in event selection criteria, $m_{\ell\ell}$ binning, slightly different calibrations, and different SM predictions also prevent a direct comparison with the value of $\sin^2 \theta_{\text{eff}}^\ell$ obtained in this analysis.

A modification of $\sin^2 \theta_{\text{eff}}^\ell$ introduces a shift in A_{FB} that is approximately linear. Consequently, it can be determined by algebraically solving the χ^2 fit, analogous to Equation 1.6. For this purpose, measurement uncertainties are included in the 51×51 covariance matrix, while PDF uncertainties are treated as nuisance parameters.

Results based on the reinterpretation of the triple-differential cross-sections measurement (Z3D) in all three channels and their combination are presented in Table 6, alongside the results of the ATLAS measurement based on A_4 . Central values in each channel differ by less than the size of the statistical uncertainty alone, an appropriate level of compatibility considering the differences in methodologies.

The discrepancy between electron and muon channel is larger in this interpretation, driven by the $80 \text{ GeV} < m_{ll} < 91 \text{ GeV}$ bins, which have the smallest uncertainties and are most strongly impacted by variations of $\sin^2 \theta_{\text{eff}}^\ell$. These bins show opposite deviations from the SM prediction in the two channels. A similar effect would be less apparent in the A_4 measurement, which jointly analyzes these events with the neighbouring bins, which tend to deviate in the opposite direction.

Statistical uncertainties of the Z3D interpretation are slightly larger, in particular in the electron channels. Two effects, which seem to cancel each other out in the muon channels, could contribute to these differences. On the one hand, the Z3D measurement has looser selection requirements. On the other hand, the fit of the angular coefficient shape of the A_4 measurement is a more powerful use of the data compared to analyzing A_{FB} only. Systematic uncertainties of the Z3D analysis are slightly larger in the muon channel, while they are compatible with the A_4 results in the electron channel. These differences could originate from different calibrations used in the ATLAS measurements or the different utilization of the data, e.g., the difference in mass binning. Despite the different PDF sets used, the presented analysis has nearly identical PDF uncertainties.

Overall, the agreement between the $\sin^2 \theta_{\text{eff}}^\ell$ interpretation presented here and the dedicated ATLAS measurement is strong, both in terms of central values and uncertainties, with some expected differences. The consistency suggests that the analysis framework can be expected to yield reasonable results in the SMEFT interpretation ahead.

3.3 General SMEFT constraints

The fit of all 30 dimension-six Wilson coefficients affecting the Z3D measurement is, like the $\sin^2 \theta_{\text{eff}}^\ell$ interpretation, performed algebraically. The nine most stringently constrained combinations of Wilson coefficients — obtained using the methodology discussed in Section 1.6 — are listed in Table 7. Constraints on additional independent directions are of least a factor of two weaker but still considered in the following analysis.

The most constrained direction corresponds to variations in both electron and muon couplings, akin to a change in $\sin^2 \theta_{\text{eff}}^\ell$. A value one-and-a-half standard deviations larger than the SM is preferred for this Wilson coefficient combination. This might seem at odds with the $\sin^2 \theta_{\text{eff}}^\ell$ measurement of 6, which is closer to the SM prediction. However, in the SMEFT fit quark coupling and four fermion operators also affect the interpretation, pulling A_{FB} in the opposite direction.

The second most tightly constrained direction aligns well with the Wilson coefficient dependence of $R_{\sin^2 \theta_{\text{eff}}^\ell}^{\mu/e}$ in Equation 2.9, confirming the power of this measurement to constrain LFU violation. The remaining directions, with constraints nearly an order of magnitude weaker, modify a mix of lepton couplings, quark couplings, and four-fermion interactions.

A good approximation of the full likelihood corresponding to the Z3D interpretation can be reconstructed from Table 7. To better understand the improvements brought by the Z3D interpretation to the set of EWPD observables, it is useful to propagate the uncertainties in Wilson coefficient to obtain uncertainties in couplings and EWPOs. In the following sections, the implied constraints on lepton and quark couplings will be discussed separately.

Constrained direction (leading contributions)	σ	Pull
$-0.66c_{HWB} - 0.58c_{HD} - 0.29c_{He,11} - 0.26c_{Hl,11}^{(3)} - 0.26c_{Hl,11}^{(1)}$	0.0098	1.5
$-0.48c_{He,22} - 0.42c_{Hl,22}^{(3)} - 0.41c_{Hl,22}^{(1)} + 0.39c_{He,11} + 0.33c_{Hl,11}^{(3)} + 0.33c_{Hl,11}^{(1)} - 0.17c_{HWB}$	0.021	-1.1
$+0.6c_{He,11} - 0.46c_{HWB} - 0.36c_{Hq}^{(3)} + 0.25c_{lj,11}^{(3)} + 0.24c_{HD} + 0.21c_{He,22} + 0.18c_{Hl,22}^{(3)}$	0.16	1.3
$+0.59c_{lj,11}^{(1)} - 0.53c_{le,11} - 0.47c_{lu,11} + 0.3c_{eu,11} + 0.15c_{ld,11} - 0.14c_{lj,11}^{(3)}$	0.26	-0.5
$-0.59c_{He,22} + 0.37c_{Hq}^{(1)} - 0.29c_{Hl,11}^{(3)} - 0.29c_{Hl,11}^{(1)} + 0.25c_{lj,11}^{(3)} + 0.25c_{He,11} + 0.2c_{Hl,22}^{(3)}$	0.4	-0.1
$-0.61c_{Hq}^{(1)} + 0.48c_{Hu} + 0.34c_{lj,11}^{(3)} + 0.25c_{eu,11} - 0.25c_{He,22} + 0.21c_{lj,11}^{(1)} + 0.17c_{HWB}$	0.58	-0.9
$+0.53c_{lu,11} + 0.44c_{lj,11}^{(3)} + 0.41c_{lj,11}^{(1)} + 0.39c_{Hq}^{(1)} + 0.3c_{eu,11} - 0.2c_{ld,11} - 0.17c_{Hu}$	1.1	-1.1
$+0.61c_{Hu} + 0.41c_{Hq}^{(1)} - 0.25c_{lj,11}^{(3)} + 0.24c_{lu,11} - 0.23c_{eu,11} - 0.23c_{Hq}^{(3)} + 0.21c_{ed,11}$	1.8	-0.3
$-0.47c_{lj,11}^{(1)} - 0.36c_{ed,11} - 0.36c_{lu,11} + 0.34c_{eu,11} + 0.33c_{Hq}^{(1)} + 0.29c_{Hu} + 0.26c_{lj,11}^{(3)}$	2.5	-0.8

Table 7. Uncorrelated linear combinations of Wilson coefficients constrained by the Drell–Yan triple-differential cross-section measurement, for $\Lambda = 1$ TeV. The linear combinations are normalized and at most six Wilson coefficients with the largest absolute value are shown, if the absolute value is larger than 0.1. The uncertainty σ corresponds to 68% confidence level intervals. The pull is defined as the best-fit value of the Wilson coefficient direction, determined by a global minimization of the χ^2 , divided by the uncertainty σ .

3.4 Constraints on lepton couplings

Constraints on the differences of the Z boson couplings of electrons and muons are derived from the general fit results using Gaussian error propagation and the formulas in Equation 2.6 and Equation 2.7. The constraints obtained are illustrated in the left-hand plot of Figure 8. The A_{FB} measurement can indeed constrain lepton couplings, even when allowing all relevant dimension-six operators to vary. As discussed in Section 2.3, A_{FB} is in particular sensitive to the difference in vector couplings, $g_V^{Z\mu} - g_V^{Ze}$, with minimal sensitivity to axial vector couplings. A combination with the LEP+SLD fit, also shown in Figure 8, leverages the strength of each measurement: the Z3D analysis provides better constraints on vector couplings, while at LEP and SLD partial width measurements pin down axial vector couplings.

The difference in vector couplings $g_V^{Z\mu} - g_V^{Ze}$, assuming SM axial vector couplings, is compared for different scenarios in Table 8. The presence of four-fermion operators, which can also violate LFU, leads to only a slight increase in uncertainty, as these operators are constrained in high-mass bins. However, as they are not constrained to zero, they introduce a significant shift of the central value.

It is instructive to compare the measurement using central–central lepton channels only with an estimate based on $R_{\sin^2 \theta_{\text{eff}}^{\ell}}^{\mu/e}$. The latter yields, based on Table 6, $g_V^{Z\mu} - g_V^{Ze} = (-13 \pm 17) \times 10^{-4}$, which is already close to the SMEFT fit without four-fermion operators presented in Table 8. When PDFs are fixed to their central values, the estimate based on $R_{\sin^2 \theta_{\text{eff}}^{\ell}}^{\mu/e}$ matches exactly the SMEFT fit result. This suggests that the difference arises from different pulls of the PDFs in the individual channels, highlighting the importance of extracting $R_{\sin^2 \theta_{\text{eff}}^{\ell}}^{\mu/e}$ in a simultaneous fit of all channels. The close agreement of the $R_{\sin^2 \theta_{\text{eff}}^{\ell}}^{\mu/e}$ estimate and the full SMEFT fit confirms that the reinterpretation of $\sin^2 \theta_{\text{eff}}^{\ell}$ as

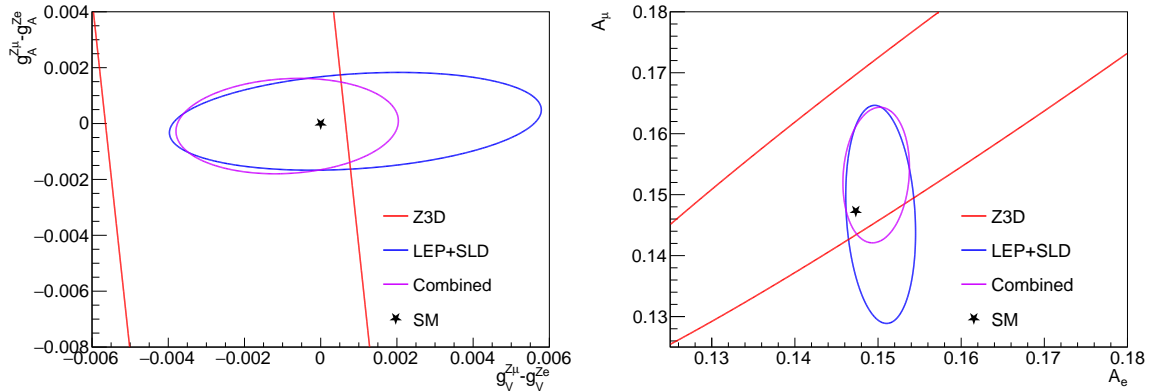


Figure 8. Constraints on the difference in muon and electron vector and axial vector couplings (left) and the asymmetry parameters A_μ and A_e (right), at 95% CL. They are derived from a SMEFT fit involving all relevant Wilson coefficients. Constraints labeled “Z3D” correspond to the re-analysis of the Drell–Yan triple-differential cross-section measurement, while LEP+SLD refers to the EWPD fit discussed in Section 1. For the coupling measurement, only one degree of freedom is constrained by the Z3D measurement and the corresponding confidence intervals are based on a one-dimensional χ^2 distribution.

Channels analyzed	Assumption	$g_V^{Z\mu} - g_V^{Ze}$ [10^{-4}]
$\mu^+\mu^-CC+e^+e^-CC+e^+e^-CF$	–	-25 ± 16
$\mu^+\mu^-CC+e^+e^-CC+e^+e^-CF$	No four-fermion operators	-18 ± 16
$\mu^+\mu^-CC+e^+e^-CC$	–	-29 ± 18
$\mu^+\mu^-CC+e^+e^-CC$	No four-fermion operators	-16 ± 17

Table 8. Comparison of 68% CL vector coupling constraints $g_V^{Z\mu} - g_V^{Ze}$ from the SMEFT fit to the ATLAS Drell–Yan triple-differential cross-section measurement in different scenarios. CC (CF) refers to central–central (central–forward) lepton channels. For these results $g_A^{Z\mu} - g_A^{Ze}$ is fixed to zero while all other Wilson coefficient combinations are allowed to vary.

a ratio measurement holds fairly general validity in the SMEFT. The shift introduced by four-fermion operators, which the $R_{\sin^2\theta_{\text{eff}}}^{\mu/e}$ estimate cannot account for, is a challenge for this approximation. However, such large four-fermion operator contributions would impact the A_{FB} of Drell–Yan production much more significantly at masses higher than those studied in this analysis. The absence of reported excesses at high mass suggests that any modifications are indeed small.

Finally, the SMEFT analysis also improves the precision of the asymmetry parameter A_μ with respect to the EWPD fit in Section 1.6. The constraints on A_μ and A_e from the SMEFT fit are shown in the right-hand plot of Figure 8. Due to unknown quark couplings, which simultaneously shift A_{FB} in both electron and muon channels, the constraints on A_μ and A_e are highly correlated. As shown in the figure, combining the SMEFT results with the LEP+SLD likelihood yields an improved result for A_μ , benefiting from the tight constraints on A_e provided by LEP and SLD.

3.5 Constraints on quark couplings

The A_{FB} measurement can also constrain quark couplings within a general SMEFT fit, using lepton coupling constraints from LEP and SLD in a global combination. While the sensitivity to quark couplings is weaker than that to lepton couplings, as the latter benefit from the accidentally small SM value of g_V^ℓ , it is of great importance. Firstly, A_{FB} at a hadron colliders offers unique sensitivity to up quarks and down quarks. This sensitivity as highlighted in Ref. [62] and estimated under simplified assumptions using the ATLAS A_4 measurement [73]. Couplings to light quark are otherwise weakly constrained from precision measurements, as only charm quarks and bottom quarks can be reliably identified experimentally. Secondly, the quark couplings that have been precisely measured in the past, i.e., those of charm quarks and bottom quarks, are in tensions with the SM. In particular, deviations in the bottom quark asymmetries A_b and $A_{\text{FB}}^{0,b}$ result in a three standard deviation discrepancy from the SM in the SMEFT fit, as shown in Table 4.

Visualizing constraints on light quark couplings is challenging because A_{FB} at the LHC only reflects the combined effects of up and down quark couplings. The asymmetry is thus affected by four degrees of freedom: the vector and axial vector couplings of the two quark flavours. To simplify the interpretation, the $U(2)_q \times U(2)_u \times U(2)_d$ symmetry assumption is employed, which requires identical couplings for up quarks and charm quarks as well as down quarks and strange quarks. In a combined analysis with LEP+SLD data this constrains the $\Gamma_{Z \rightarrow u\bar{u}}$ and $\Gamma_{Z \rightarrow d\bar{d}}$ partial widths, linking them to the $\Gamma_{Z \rightarrow c\bar{c}}$ and $\Gamma_{Z \rightarrow s\bar{s}}$ partial widths. This assumption essentially precludes scenarios where $\Gamma_{Z \rightarrow u\bar{u}}$ and $\Gamma_{Z \rightarrow c\bar{c}}$ differ from the SM while their sum does not, a scenario compatible with EWPD but unlikely.

With all Z boson partial width constrained by LEP and SLD data, only two light quark coupling combinations affecting A_u and A_d but not altering partial widths are unconstrained. One combination is tightly constrained by the Z3D measurement, as shown in Figure 9. The result is limited by lepton coupling uncertainties. Assuming no deviations from the SM expectation in lepton couplings, the A_u and A_d constraints of Figure 9 improve to a sensitivity that is comparable to that of A_c and A_b measurements.

Thus, future improvements in the precision of light quark constraints from A_{FB} measurement could provide insights whether quark couplings differ in general from the SM, potentially providing new insights into a longstanding discrepancy in the electroweak fit.

Conclusion

This paper presented a computer code designed to calculate the likelihood of electroweak precision data within the framework of the Standard Model Effective Field Theory. The code integrates state-of-the-art experimental and theoretical results, including next-to-leading order effects in both perturbative and SMEFT expansions. It offers five electroweak input parameter schemes and a more thorough treatment of uncertainties than previous approaches, fully accounting for the input parameter dependence of EWPO predictions. The assumptions and conventions align with those used in LHC analyses, making this code, which produces text file and `Roofit` output, ideally suited for more extensive fits that incorporate LHC data. For the first time, EWPD fits were performed and compared in five

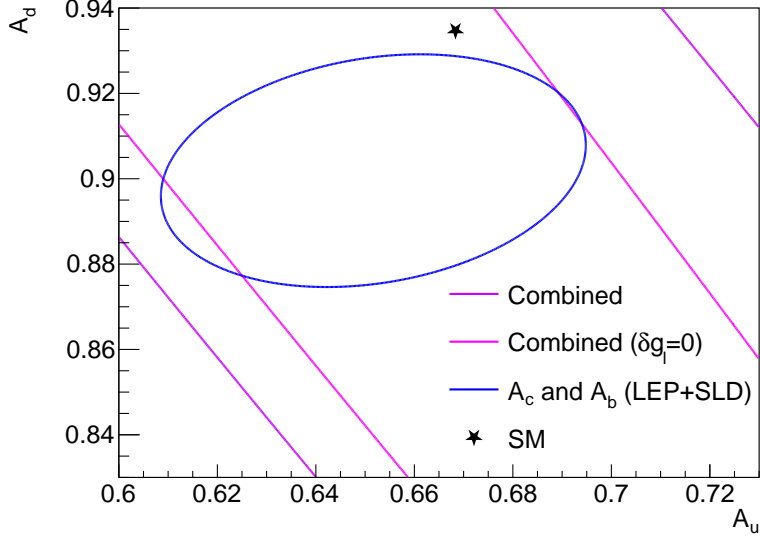


Figure 9. Constraints on the quark coupling asymmetry parameters A_u and A_d , at 95% CL. Derived from a combined SMEFT fit of EWPD and the ATLAS Drell–Yan triple-differential cross-section measurement, where all relevant dimension-six Wilson coefficients are allowed to vary. For the result labeled $\delta g_\ell = 0$, lepton couplings are fixed to their SM value. For comparison, the quark asymmetry parameters A_c and A_b from the EWPD fit of Section 1 are also shown, with A_c and A_u (A_b and A_d) sharing the coordinate axes. For the light quark measurement, only one degree of freedom is constrained. Hence, the corresponding confidence intervals are based on a one-dimensional χ^2 distribution. The indicated SM value is valid for both sets of parameters.

different input parameter schemes, at leading and next-to-leading order. The impact of next-to-leading order corrections and the scheme choice was found to be small.

The impact of recent LHC measurements on the EWPD likelihood was analyzed. The analysis demonstrated that the ATLAS measurements of the W boson mass [5] and the lepton flavor universality in W branching fractions [6] provide constraints in the SMEFT that are more precise than those obtained by fitting all prior data (if the CDF measurement of the W mass is discarded). While the same is not true for the Γ_W measurement, which leads despite its precision to only a marginal improvement in the SMEFT fit, the significance of a joint M_W - Γ_W measurement was highlighted. Furthermore, it was shown that the CMS effective leptonic weak mixing angle measurement [7] can be used to construct one of the most precise tests of LFU in weak boson couplings to date, by measuring the ratio $R_{\sin^2 \theta_{\text{eff}}^\ell}^{\mu/e}$. This was further explored through a SMEFT interpretation of an LHC Run 1 ATLAS Drell–Yan triple-differential cross-section measurement [8]. The interpretation not only validated the LFU test and improved constraints on muon couplings by nearly a factor of two but also simultaneously constrained the quark coupling asymmetry parameters A_u and A_d , providing an important cross-check of A_c and A_b measurements from LEP and SLD.

A precise measurement of $R_{\sin^2 \theta_{\text{eff}}^\ell}^{\mu/e}$ by the experimental collaborations is strongly encouraged, as it has the potential to be the most powerful test of lepton universality of weak boson couplings. The publication of CMS or ATLAS measurements of either A_{FB} or the

angular coefficient A_4 , as a function of rapidity and mass, separately for both electron and muon channels, would allow revisiting the presented SMEFT interpretation using Run 2 data. A detailed breakdown of experimental uncertainties and the publication of Standard Model predictions would be extremely valuable for this endeavor while extending the measured mass range beyond the Z pole would help constraining four-fermion operators. Ideally, such analyses should be undertaken by the experimental collaborations, which have the best understanding of experimental limitations and can optimize their measurements for the purpose of a SMEFT interpretation.

Acknowledgements

I would like to express my gratitude to Anke Biekötter, Ken Mimasu, and Matthias Schott for valuable discussions and comments on the manuscript. Anke Biekötter I would also like to thank for providing NLO SMEFT parametrizations in multiple input parameter schemes and for numerical comparisons. I am especially thankful to Matthias Schott for his continuous support throughout this project. I also extend my thanks to Mike Trott for his initial introduction to EWPD in the SMEFT. Support of the BMBF (Federal Ministry of Education and Research) is gratefully acknowledged.

References

- [1] W. Buchmuller and D. Wyler, *Effective Lagrangian Analysis of New Interactions and Flavor Conservation*, *Nucl. Phys. B* **268** (1986) 621.
- [2] B. Grzadkowski, M. Iskrzynski, M. Misiak and J. Rosiek, *Dimension-Six Terms in the Standard Model Lagrangian*, *JHEP* **10** (2010) 085 [[1008.4884](#)].
- [3] I. Brivio and M. Trott, *The Standard Model as an Effective Field Theory*, *Phys. Rept.* **793** (2019) 1 [[1706.08945](#)].
- [4] ALEPH, DELPHI, L3, OPAL, SLD, LEP ELECTROWEAK WORKING GROUP, SLD ELECTROWEAK GROUP, SLD HEAVY FLAVOUR GROUP collaboration, *Precision electroweak measurements on the Z resonance*, *Phys. Rept.* **427** (2006) 257 [[hep-ex/0509008](#)].
- [5] ATLAS collaboration, *Measurement of the W-boson mass and width with the ATLAS detector using proton-proton collisions at $\sqrt{s} = 7$ TeV*, [2403.15085](#).
- [6] ATLAS collaboration, *Precise test of lepton flavour universality in W-boson decays into muons and electrons in pp collisions at $\sqrt{s} = 13$ TeV with the ATLAS detector*, *Eur. Phys. J. C* **84** (2024) 993 [[2403.02133](#)].
- [7] CMS collaboration, *Measurement of the Drell–Yan forward-backward asymmetry and of the effective leptonic weak mixing angle in proton-proton collisions at $\sqrt{s} = 13$ TeV*, [2408.07622](#).
- [8] ATLAS collaboration, *Measurement of the Drell–Yan triple-differential cross section in pp collisions at $\sqrt{s} = 8$ TeV*, *JHEP* **12** (2017) 059 [[1710.05167](#)].
- [9] Z. Han and W. Skiba, *Effective theory analysis of precision electroweak data*, *Phys. Rev. D* **71** (2005) 075009 [[hep-ph/0412166](#)].
- [10] A. Pomarol and F. Riva, *Towards the Ultimate SM Fit to Close in on Higgs Physics*, *JHEP* **01** (2014) 151 [[1308.2803](#)].

- [11] A. Falkowski and F. Riva, *Model-independent precision constraints on dimension-6 operators*, *JHEP* **02** (2015) 039 [[1411.0669](#)].
- [12] A. Efrati, A. Falkowski and Y. Soreq, *Electroweak constraints on flavorful effective theories*, *JHEP* **07** (2015) 018 [[1503.07872](#)].
- [13] L. Berthier and M. Trott, *Consistent constraints on the Standard Model Effective Field Theory*, *JHEP* **02** (2016) 069 [[1508.05060](#)].
- [14] J. de Blas, M. Ciuchini, E. Franco, S. Mishima, M. Pierini, L. Reina et al., *The Global Electroweak and Higgs Fits in the LHC era*, *PoS EPS-HEP2017* (2017) 467 [[1710.05402](#)].
- [15] E. da Silva Almeida, A. Alves, N. Rosa Agostinho, O.J.P. Éboli and M.C. Gonzalez-Garcia, *Electroweak Sector Under Scrutiny: A Combined Analysis of LHC and Electroweak Precision Data*, *Phys. Rev. D* **99** (2019) 033001 [[1812.01009](#)].
- [16] A. Biekötter, T. Corbett and T. Plehn, *The Gauge-Higgs Legacy of the LHC Run II*, *SciPost Phys.* **6** (2019) 064 [[1812.07587](#)].
- [17] J. Aebischer, J. Kumar, P. Stangl and D.M. Straub, *A Global Likelihood for Precision Constraints and Flavour Anomalies*, *Eur. Phys. J. C* **79** (2019) 509 [[1810.07698](#)].
- [18] J. Ellis, C.W. Murphy, V. Sanz and T. You, *Updated Global SMEFT Fit to Higgs, Diboson and Electroweak Data*, *JHEP* **06** (2018) 146 [[1803.03252](#)].
- [19] A. Falkowski and D. Straub, *Flavourful SMEFT likelihood for Higgs and electroweak data*, *JHEP* **04** (2020) 066 [[1911.07866](#)].
- [20] T. Corbett, A. Helset, A. Martin and M. Trott, *EWPD in the SMEFT to dimension eight*, *JHEP* **06** (2021) 076 [[2102.02819](#)].
- [21] L. Bellafrente, S. Dawson and P.P. Giardino, *The importance of flavor in SMEFT Electroweak Precision Fits*, *JHEP* **05** (2023) 208 [[2304.00029](#)].
- [22] E. Celada, T. Giani, J. ter Hoeve, L. Mantani, J. Rojo, A.N. Rossia et al., *Mapping the SMEFT at high-energy colliders: from LEP and the (HL-)LHC to the FCC-ee*, *JHEP* **09** (2024) 091 [[2404.12809](#)].
- [23] ATLAS collaboration, *Combined effective field theory interpretation of Higgs boson and weak boson production and decay with ATLAS data and electroweak precision observables*, ATLAS PUB Note [ATL-PHYS-PUB-2022-037](#) (2022).
- [24] CMS collaboration, *Combined effective field theory interpretation of Higgs boson, electroweak vector boson, top quark, and multi-jet measurements*, CMS Physics Analysis Summary [CMS-PAS-SMP-24-003](#) (2024).
- [25] W. Verkerke and D.P. Kirkby, *The RooFit toolkit for data modeling*, [physics/0306116](#).
- [26] I. Brivio, S. Dawson, J. de Blas, G. Durieux, P. Savard, A. Denner et al., *Electroweak input parameters*, [2111.12515](#).
- [27] I. Brivio, Y. Jiang and M. Trott, *The SMEFTsim package, theory and tools*, *JHEP* **12** (2017) 070 [[1709.06492](#)].
- [28] I. Brivio, *SMEFTsim 3.0 — a practical guide*, *JHEP* **04** (2021) 073 [[2012.11343](#)].
- [29] S. Dawson and P.P. Giardino, *Electroweak and QCD corrections to Z and W pole observables in the standard model EFT*, *Phys. Rev. D* **101** (2020) 013001 [[1909.02000](#)].

- [30] S. Dawson and P.P. Giardino, *Flavorful electroweak precision observables in the Standard Model effective field theory*, *Phys. Rev. D* **105** (2022) 073006 [2201.09887].
- [31] A. Biekötter, B.D. Pecjak, D.J. Scott and T. Smith, *Electroweak input schemes and universal corrections in SMEFT*, *JHEP* **07** (2023) 115 [2305.03763].
- [32] A. Biekötter, B.D. Pecjak and T. Smith, *Using the effective weak mixing angle as an input parameter in SMEFT*, *JHEP* **04** (2024) 073 [2312.08446].
- [33] A. Helset, A. Martin and M. Trott, *The Geometric Standard Model Effective Field Theory*, *JHEP* **03** (2020) 163 [2001.01453].
- [34] Y. Liu, Y. Wang, C. Zhang, L. Zhang and J. Gu, *Probing top-quark operators with precision electroweak measurements**, *Chin. Phys. C* **46** (2022) 113105 [2205.05655].
- [35] D. Barducci et al., *Interpreting top-quark LHC measurements in the standard-model effective field theory*, [1802.07237](#).
- [36] P. Janot and S. Jadach, *Improved Bhabha cross section at LEP and the number of light neutrino species*, *Phys. Lett. B* **803** (2020) 135319 [1912.02067].
- [37] PARTICLE DATA GROUP collaboration, *Review of particle physics*, *Phys. Rev. D* **110** (2024) 030001.
- [38] ATLAS collaboration, *Precision measurement and interpretation of inclusive W^+ , W^- and Z/γ^* production cross sections with the ATLAS detector*, *Eur. Phys. J. C* **77** (2017) 367 [1612.03016].
- [39] ATLAS collaboration, *Test of the universality of τ and μ lepton couplings in W -boson decays with the ATLAS detector*, *Nature Phys.* **17** (2021) 813 [2007.14040].
- [40] CMS collaboration, *Precision measurement of the W boson decay branching fractions in proton-proton collisions at $\sqrt{s} = 13$ TeV*, *Phys. Rev. D* **105** (2022) 072008 [2201.07861].
- [41] LHCb collaboration, *Measurement of forward $W \rightarrow e\nu$ production in pp collisions at $\sqrt{s} = 8$ TeV*, *JHEP* **10** (2016) 030 [1608.01484].
- [42] CDF collaboration, *High-precision measurement of the W boson mass with the CDF II detector*, *Science* **376** (2022) 170.
- [43] CMS collaboration, *Measurement of the W boson mass in proton-proton collisions at $\sqrt{s} = 13$ TeV*, CMS Physics Analysis Summary [CMS-PAS-SMP-23-002](#) (2024).
- [44] M. Davier, A. Hoecker, B. Malaescu and Z. Zhang, *A new evaluation of the hadronic vacuum polarisation contributions to the muon anomalous magnetic moment and to $\alpha(m_Z^2)$* , *Eur. Phys. J. C* **80** (2020) 241 [1908.00921].
- [45] M. Steinhauser, *Leptonic contribution to the effective electromagnetic coupling constant up to three loops*, *Phys. Lett. B* **429** (1998) 158 [hep-ph/9803313].
- [46] E. Celada, G. Durieux, K. Mimasu and E. Vryonidou, *Triboson production in the SMEFT*, [2407.09600](#).
- [47] I. Brivio and M. Trott, *Scheming in the SMEFT... and a reparameterization invariance!*, *JHEP* **07** (2017) 148 [1701.06424].
- [48] FLAVOUR LATTICE AVERAGING GROUP (FLAG) collaboration, *FLAG Review 2021*, *Eur. Phys. J. C* **82** (2022) 869 [2111.09849].
- [49] M. Trott, *α_s as an input parameter in the SMEFT*, [2306.14784](#).

- [50] A.H. Hoang, *What is the Top Quark Mass?*, *Ann. Rev. Nucl. Part. Sci.* **70** (2020) 225 [[2004.12915](#)].
- [51] I. Dubovyk, A. Freitas, J. Gluza, T. Riemann and J. Usovitsch, *Electroweak pseudo-observables and Z-boson form factors at two-loop accuracy*, *JHEP* **08** (2019) 113 [[1906.08815](#)].
- [52] M. Awramik, M. Czakon and A. Freitas, *Electroweak two-loop corrections to the effective weak mixing angle*, *JHEP* **11** (2006) 048 [[hep-ph/0608099](#)].
- [53] M. Awramik, M. Czakon, A. Freitas and G. Weiglein, *Precise prediction for the W boson mass in the standard model*, *Phys. Rev. D* **69** (2004) 053006 [[hep-ph/0311148](#)].
- [54] G.-C. Cho, K. Hagiwara, Y. Matsumoto and D. Nomura, *The MSSM confronts the precision electroweak data and the muon $g-2$* , *JHEP* **11** (2011) 068 [[1104.1769](#)].
- [55] J. Haller, A. Hoecker, R. Kogler, K. Mönig and J. Stelzer, *Status of the global electroweak fit with Gfitter in the light of new precision measurements*, *PoS ICHEP2022* (2022) 897 [[2211.07665](#)].
- [56] J. Alwall, R. Frederix, S. Frixione, V. Hirschi, F. Maltoni, O. Mattelaer et al., *The automated computation of tree-level and next-to-leading order differential cross sections, and their matching to parton shower simulations*, *JHEP* **07** (2014) 079 [[1405.0301](#)].
- [57] J. Alwall, C. Duhr, B. Fuks, O. Mattelaer, D.G. Öztürk and C.-H. Shen, *Computing decay rates for new physics theories with FeynRules and MadGraph 5_aMC@NLO*, *Comput. Phys. Commun.* **197** (2015) 312 [[1402.1178](#)].
- [58] L. Berthier, M. Bjørn and M. Trott, *Incorporating doubly resonant W^\pm data in a global fit of SMEFT parameters to lift flat directions*, *JHEP* **09** (2016) 157 [[1606.06693](#)].
- [59] F. Maltoni et al., *Proposal for the validation of Monte Carlo implementations of the standard model effective field theory*, [1906.12310](#).
- [60] T. Corbett, *The Feynman rules for the SMEFT in the background field gauge*, *JHEP* **03** (2021) 001 [[2010.15852](#)].
- [61] CMS collaboration, *Search for physics beyond the standard model in top quark production with additional leptons in the context of effective field theory*, *JHEP* **12** (2023) 068 [[2307.15761](#)].
- [62] V. Bresó-Pla, A. Falkowski and M. González-Alonso, *A_{FB} in the SMEFT: precision Z physics at the LHC*, *JHEP* **08** (2021) 021 [[2103.12074](#)].
- [63] ALEPH, DELPHI, L3, OPAL, LEP ELECTROWEAK collaboration, *Electroweak Measurements in Electron-Positron Collisions at W-Boson-Pair Energies at LEP*, *Phys. Rept.* **532** (2013) 119 [[1302.3415](#)].
- [64] D0 collaboration, *Measurement of the W boson mass with the D0 detector*, *Phys. Rev. D* **89** (2014) 012005 [[1310.8628](#)].
- [65] LHCb collaboration, *Measurement of the W boson mass*, *JHEP* **01** (2022) 036 [[2109.01113](#)].
- [66] ATLAS collaboration, *Measurement of the W-boson mass in pp collisions at $\sqrt{s} = 7$ TeV with the ATLAS detector*, *Eur. Phys. J. C* **78** (2018) 110 [[1701.07240](#)].
- [67] LHC-TeV MW WORKING GROUP collaboration, *Compatibility and combination of world W-boson mass measurements*, *Eur. Phys. J. C* **84** (2024) 451 [[2308.09417](#)].

- [68] M. Bjørn and M. Trott, *Interpreting W mass measurements in the SMEFT*, *Phys. Lett. B* **762** (2016) 426 [[1606.06502](#)].
- [69] CMS collaboration, *Measurement of the weak mixing angle with the Drell-Yan process in proton-proton collisions at the LHC*, *Phys. Rev. D* **84** (2011) 112002 [[1110.2682](#)].
- [70] S. Alioli, P. Nason, C. Oleari and E. Re, *A general framework for implementing NLO calculations in shower Monte Carlo programs: the POWHEG BOX*, *JHEP* **06** (2010) 043 [[1002.2581](#)].
- [71] L. Barze, G. Montagna, P. Nason, O. Nicrosini and F. Piccinini, *Implementation of electroweak corrections in the POWHEG BOX: single W production*, *JHEP* **04** (2012) 037 [[1202.0465](#)].
- [72] NNPDF collaboration, *Parton distributions from high-precision collider data*, *Eur. Phys. J. C* **77** (2017) 663 [[1706.00428](#)].
- [73] ATLAS collaboration, *Measurement of the effective leptonic weak mixing angle using electron and muon pairs from Z -boson decay in the ATLAS experiment at $\sqrt{s} = 8$ TeV*, ATLAS CONF Note [ATLAS-CONF-2018-037](#) (2018).
- [74] ATLAS collaboration, *Measurement of the associated production of a Higgs boson decaying into b -quarks with a vector boson at high transverse momentum in pp collisions at $\sqrt{s} = 13$ TeV with the ATLAS detector*, *Phys. Lett. B* **816** (2021) 136204 [[2008.02508](#)].

A Appendix: How to run the code

The code is available for download at:

<https://github.com/ewpd4lhc/ewpd4lhc>

It requires `python3` with the `numpy` and `yaml` modules. A `ROOT` installation with `python` bindings is required for `Roofit` output and workspace manipulation. On CERN LXPLUS, no preparation is required as all of these requirements are met.

In the configuration file `config/ewpd4lhc.cfg` one can modify:

- The list of observables included in the likelihood.
- The input scheme for calculations (see Table 1).
- The treatment of theoretical and parametric uncertainties (either as part of the covariance of the multivariate Gaussian or as nuisance parameters, see Section 1.3)
- The SMEFT symmetry assumption (see also Table 1).
- Optionally, a subset of Wilson coefficients to be included.
- The source of dimension-six linear, dimension-six squared, and dimension-eight parametrizations (see also Table 1).

Measurement data, which may be adapted by the user, is stored as `yaml` files in the `data` folder with multiple alternative SMEFT parametrizations stored in the same location.

A `yaml` output file describing the SMEFT EWPD likelihood can be created by running the main executable:

```
./ewpd4lhc.py
```

where by default `input/ewpo.cfg` is taken as input and the SMEFT likelihood is stored in a textfile name `ewpd_out.yaml`. Alternative predefined configuration files can be found in the same folder. The output describes the multivariate Gaussian model: The predicted values of all observables, the total uncertainty — possibly including theory and parametrization as sources of uncertainties — and correlation, the Wilson coefficient dependence, and possibly the dependence of SM predictions on input parameters as well as theory nuisance parameters. During the execution of the tool, SM and SMEFT fits are performed and the results printed.

Optional arguments can be listed with:

```
./ewpd4lhc.py --help
```

For example, a `ROOT` workspace can be created either directly:

```
./ewpd4lhc.py --root_output ROOTFILENAME.root
```

Or in a separate step from the output textfile (allowing the user to modify or build more complex likelihoods) with:

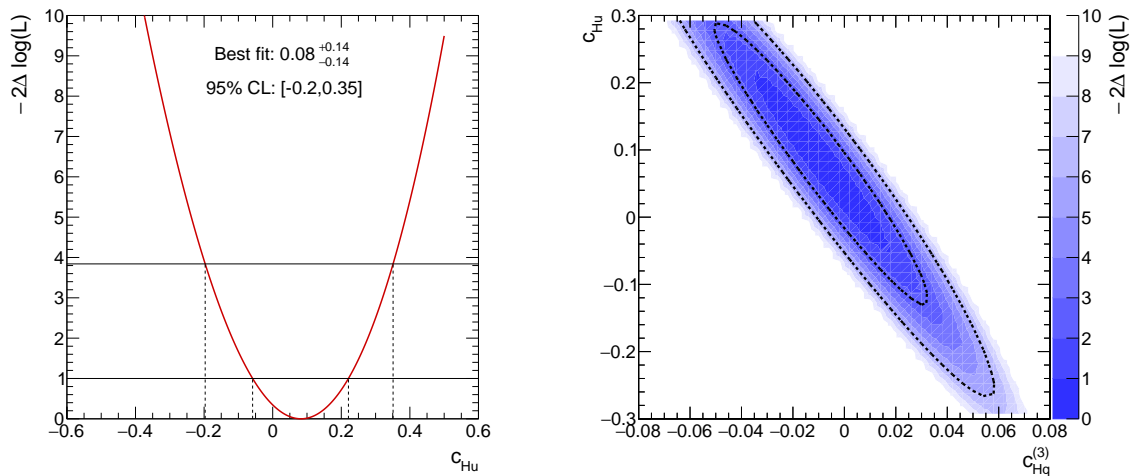


Figure 10. Examples of likelihood scans performed with `ewpd4lhc`. In the left plot, c_{Hu} is varied and $c_{Hq}^{(3)}$ is left floating in the fit. In the right plot, both parameters are scanned. The corresponding commands can be found in the main text.

```
./ewpd4lhc.py --output YAMLFILE.yml
./yaml2root.py --input YAMLFILE.yml --output ROOTFILENAME.root
```

A simple script for fitting the ROOT output is part of the code, too. Workspace contents are printed with:

```
./ROOTfit/fit.py --input ROOTFILENAME.root
```

A fit of one or multiple parameters of interest is performed, e.g., with:

```
./ROOTfit/fit.py --input ROOTFILENAME.root --pois=cHu,cHd,cHj3,cHj1
```

It is possible to specify `--poi=all` but this will usually not converge without extra constraints as the EWPD likelihood is degenerate. One- and two-dimensional scans of the likelihood can be performed with the following commands, with scan points being stored in a textfile and optionally being plotted as pdf graphics. Wilson coefficients other than the POIs can be required to “float” in the fit, in which case they are set to the value that maximized the likelihood at each scan point.

```
./ROOTfit/fit.py --input ROOTFILENAME.root --pois=cHu \
  --scan=-0.1:0.1 --outfolder=1Dscan --plot
./ROOTfit/fit.py --input ROOTFILENAME.root --pois=cHu \
  --scan=-0.5:0.5 --float=cHj3 --outfolder=1DscanProfiled --plot
./ROOTfit/fit.py --input ROOTFILENAME.root --pois=cHj3,cHu \
  --scan=-0.08:0.08,-0.3:0.3 --outfolder=2Dscan --plot --npoints=300
```

The pdf output of the second and third command is shown in Figure 10. It can, for example, be compared to Figure 18 of the auxiliary material of Ref. [74], showing a complementarity

between LHC Higgs measurements and EWPD – that is however best explored by combining the `ewpd4lhc` workspace with the ATLAS workspace.

The low level classes like `SMcalculator`, `SMEFTlikelihood`, and `LINAFit` can also be used directly in python. For example:

```
import SMcalculator
sm=SMcalculator.EWPOcalculator(MH=125.25,
                               mt=172.69,
                               alphas=0.118,
                               MZ=91.1875,
                               MW=80.377)

print('AFBb:',sm.AFBb())
sm.update(MW=80.3)
print('AFBb(MW=80.3):',sm.AFBb())
sm.reset()
print('Also AFBb:',sm.get('AFBb'))
print('dAFBb/dMW:',sm.derivative('AFBb','MW'))
print('All observables:', sm.getall())
```

Finally, `MG5_aMC`-based parametrizations can be generated using the code in the `ParaFactory` subfolder.